

AUTOMATIC MINIRHIZOTRON ROOT IMAGE
ANALYSIS USING TWO-DIMENSIONAL MATCHED
FILTERING AND LOCAL ENTROPY THRESHOLDING

A Thesis
Presented to
the Graduate School of
Clemson University

In Partial Fulfillment
of the Requirements for the Degree
Master of Science
Electrical Engineering

by
Guang Zeng
May 2005

Advisor: Dr. Stan Birchfield

May 6, 2005

To the Graduate School:

This thesis entitled “Automatic Minirhizotron Root Image Analysis Using Two-Dimensional Matched Filtering and Local Entropy Thresholding” and written by Guang Zeng is presented to the Graduate School of Clemson University. I recommend that it be accepted in partial fulfillment of the requirements for the degree of Master of Science with a major in Electrical Engineering.

Dr. Stan Birchfield, Advisor

We have reviewed this thesis
and recommend its acceptance:

Dr. Adam W. Hoover

Dr. Ian D. Walker

Accepted for the Graduate School:

ABSTRACT

An approach to automate the procedure of extracting and measuring roots in minirhizotron images is presented. By the use of two-dimensional matched filtering and local entropy thresholding, one can efficiently enhance the local contrast of the root and then extract it from the minirhizotron image. We also present several techniques for discriminating roots against extraneous objects based on their geometric features and intensity distribution properties. Once the root is detected, its length is estimated as the length of the medial axis using a more accurate length estimator based on Kimura's method. Experimental results on a large number of images show that our automatic approach can successfully extract and measure different types of root in different kinds of soil, as well as discriminate between genuine roots and bright extraneous objects.

DEDICATION

I dedicate this work to my parents and my two sisters Yue and Ming.

ACKNOWLEDGMENTS

I am indebted to my advisor Dr. Stan Birchfield for his invaluable guidance, understanding and help during the last two years. I also thank him for supporting me as a research assistant during this period.

I wish to thank Dr. Adam Hoover and Dr. Ian Walker for agreeing to serve on my Master's examination committee.

Most importantly, I would like to thank my friend, Hong, for her tremendous love and support.

TABLE OF CONTENTS

	Page
TITLE PAGE	i
ABSTRACT	ii
DEDICATION	iii
LIST OF TABLES	vi
LIST OF FIGURES	vii
1 Introduction	1
1.1 Overview of Approach	4
1.2 Related Work	4
1.3 Thesis Statement	7
1.4 Thesis Organization	8
2 Approach	9
2.1 Preprocessing	9
2.2 Matched Filtering	13
2.3 Local Entropy Thresholding	14
2.4 Root Selecting	24
2.5 Root Measuring	27
3 Root Discrimination	33
3.1 Eccentricity	33
3.2 Approximate Line Symmetry	34
3.3 Boundary Parallelism	36
3.4 Histogram Distribution	36
3.5 Edge Detection	38
3.6 Optimal Threshold Selecting	39
4 Experimental Results	40
5 Conclusion	65

LIST OF TABLES

Table	Page
2.1	Root candidate selecting from Figure. 2.14. Here the area size filter is 13456. 27
4.1	Comparison among these three methods. 59
4.2	TPR and FPR of the five methods at the optimal thresholding point. 62
4.3	The distances between the optimal threshold point of the five methods to the ideal point (0,1). 64

LIST OF FIGURES

Figure	Page
1.1 An example minirhizotron system	3
2.1 The schematic diagram of the algorithm	10
2.2 RGB color image and its three components in grayscale	11
2.3 A root image and its preprocessing result: (a) The original RGB color image. (b) The green component of image. (c) The preprocessed image.	12
2.4 A cross section of the root in the preprocessed image (left) and its gray level intensity profile (right)	13
2.5 A sample kernel along 180° . (81×81)	15
2.6 Four matched filter kernels and their application results. Left column: The matched filter kernel; Middle column: The full size MFR image; Right column: The half size MFR image. (Scaled for display)	16
2.7 Top row: Two different images with the same histogram. The gray levels of the pixels are 51, 153 and 255 respectively in the center square, the four small squares and the outer border. Bottom row: The gray level histogram.	17
2.8 A 3×3 matrix (left) and its co-occurrence matrix (right).	18
2.9 The 2D histogram of the two images in Figure 2.7.	20
2.10 Quadrants of the co-occurrence matrix	21
2.11 Selecting the optimal threshold for object-background classification of the two images in Figure 2.7.	22
2.12 The corresponding LET output of the MFR images in Figure. 2.6.	23
2.13 A comparison between the LET outputs of these two different schemes.	25
2.14 The root candidates selected from the thresholded images in Fig. 2.7;	26
2.15 The output of root selecting	27
2.16 The one-pixel-wide skeleton of a smooth root	28
2.17 An example of finding medial axis of root from its skeleton tree. (a) The skeleton tree of a root caused by slight irregularities in the shape, (b) The found medial axis from the skeleton tree using Dijkstra's algorithm.	28

2.18	(a) A single line medial axis is represented as meshed pixels. An open circle shows a diagonally connected pair of pixel and a closed circle shows an orthogonally connected pair of pixels. (b) Freeman formula estimates the actual root length as the length of the dash line. (c) The line AB is the oblique side of a right angle triangle ABC. The open and closed circles are arranged that the length of AC is defined as N_d and that of BC is defined as N_d plus N_o . Pythagorean theorem estimates the actual length of the root as the length of AB. (d) A two-line medial axis is represented as meshed pixels. Pythagorean theorem estimates the actual length of the two lines AF and FB as the length of AB, while $AB < AF + FB$	30
2.19	(a) Kimura's method estimates the actual length of AB as the length of two lines AE and EB. The length of AE is calculated by applying the Pythagorean theorem to right triangle AEC. (b) Kimura's method estimates the actual length of the two lines AF and FB as the length of the two virtual lines AE and EB.	31
2.20	An Examples of root measurement.	32
3.1	Examples of falsely detected root. First row: A falsely detected root caused by a bright extraneous object; Second row: A falsely detected root caused by the uneven diffusion of light through the minirhizotron wall.	34
3.2	An example of discriminating root by detecting its eccentricity	35
3.3	An example of classifying an object by detecting its approximate line symmetry. (a) an approximate line symmetrical root; (b) an unsymmetrical no-root object.	35
3.4	An example of histogram distribution method: (a) The outline of a detected root in original grayscale image; (b) The histogram of the root; (c) The outline of a no-root object in original grayscale image; (d) The histogram of the no-root object.	37
3.5	An example of edge detection method: (a) The detected edge points inside a root; (b) The detected edge points inside a no-root object.	38
4.1	The results of applying our approach to 12 sample images. First row: Input Image and Extracted root; Second row: Hand-labeled medial axis and measured root.	41
4.1	The results of applying our approach to 12 sample images. First row: Input Image and Extracted root; Second row: Hand-labeled medial axis and measured root. (cont.)	42
4.1	The results of applying our approach to 12 sample images. First row: Input Image and Extracted root; Second row: Hand-labeled medial axis and measured root. (cont.)	43
4.1	The results of applying our approach to 12 sample images. First row: Input Image and Extracted root; Second row: Hand-labeled medial axis and measured root. (cont.)	44

4.1	The results of applying our approach to 12 sample images. First row: Input Image and Extracted root; Second row: Hand-labeled medial axis and measured root. (cont.)	45
4.1	The results of applying our approach to 12 sample images. First row: Input Image and Extracted root; Second row: Hand-labeled medial axis and measured root. (cont.)	46
4.1	The results of applying our approach to 12 sample images. First row: Input Image and Extracted root; Second row: Hand-labeled medial axis and measured root. (cont.)	47
4.1	The results of applying our approach to 12 sample images. First row: Input Image and Extracted root; Second row: Hand-labeled medial axis and measured root. (cont.)	48
4.1	The results of applying our approach to 12 sample images. First row: Input Image and Extracted root; Second row: Hand-labeled medial axis and measured root. (cont.)	49
4.1	The results of applying our approach to 12 sample images. First row: Input Image and Extracted root; Second row: Hand-labeled medial axis and measured root. (cont.)	50
4.1	The results of applying our approach to 12 sample images. First row: Input Image and Extracted root; Second row: Hand-labeled medial axis and measured root. (cont.)	51
4.1	The results of applying our approach to 12 sample images. First row: Input Image and Extracted root; Second row: Hand-labeled medial axis and measured root. (cont.)	52
4.2	In this MFR image, the histogram exhibits a bimodal distribution, so both of the two methods work well.	54
4.2	In this MFR image, the histogram exhibits unimodal distribution. Otsu's method fails while the LET method works well. (cont.)	55
4.2	In this MFR image, the histogram exhibits a complicated relationship between foreground and background. The output of Otsu's method has severe shape distortion, while the LET method gives a better result. (cont.)	56
4.2	In this MFR image, the histogram exhibits a complicated relationship between foreground and background. The Otsu's method fails while the LET method works well. (cont.)	57
4.3	Sample Roots used for the experiment. First row: The medial axis used for root length measurement; Second row: The hand-labeled ground truth used for reference length.	58
4.4	(a) Relationship between root length determined by Kimura's method and manual measurement; (b) Relationship between root length determined by Freeman formula and manual measurement.	59
4.5	The ROC curve and the estimated optimal thresholding value of each method.	60
4.5	The ROC curve and the estimated optimal thresholding value of each method. (cont.)	61

4.5	The ROC curve and the estimated optimal thresholding value of each method. (cont.)	62
4.6	ROC curves of the five methods	63
4.7	Examples of multiple roots detection.	64

Chapter 1

Introduction

When we walk in a botanical garden or talk about plants, we tend to concentrate on the above ground portion, such as the straight stems, the spreading branches, the lush leaves and the abundant products. However, there is another part of the plants that grows under the soil surface and is often ignored. Roots, the hidden half of the plants, serve a variety of important functions for plants. They not only provide support for the above ground portion, but also supply the plants with water and nutrients. Recently, extensive reviews in [8][19] point out that the quantification of root length, diameter, and associated surface area can help to determine the mechanisms relating root distributions to their functions. This important information improves our understanding of root dynamics and associated functions in ecological systems. Despite the great importance of roots, research on root systems faces many challenges. Perhaps the two greatest obstacles to root research are difficulties in viewing roots in situ and soil heterogeneity, which leads to large variability in repeated root observations.

Unlike the above ground plant components, roots are difficult to study because they are included in the soil, a non-transparent medium, and are not easily separated from soil. The traditional methods of root investigations are based on soil core sampling [7][16]. These methods carry out research based on cleaned root samples which are acquired after some

preliminary operations like washing root systems from soil coring and manually removing large extraneous objects. Although these methods can provide precise estimation of root morphology, they are labor-intensive and destructive.

Today, intensive and high-technology root research most frequently utilizes transparent walls or tubes for root observation. Large underground laboratories, called *rhizotrons*, have transparent-wall chambers for the observation of root growth, allowing the analysis of root growth while the aerial parts of the plant are exposed to natural field conditions. In a rhizotron, grid lines on the transparent walls indicate soil depth. Details of root morphology (root size and distribution) under natural growing conditions can be observed with specially designed microscopes, mounted adjacent to the transparent walls of the root chambers. Because rhizotrons are expensive to construct and maintain, they have been largely supplanted by *minirhizotrons*. Minirhizotrons are transparent plastic tubes buried at an angle in the soil near the plants to be observed. Rhizotron and minirhizotron observations are nondestructive, thereby allowing repeated in-situ observations and measurements with little disturbance to the natural environment.

Originally, an optical device such as a tilted mirror with a magnifying lens is inserted into the minirhizotron tube to monitor roots growing along its surface. Upchurch and Ritchie provide a promising method [30] by inserting a miniature video camera into the minirhizotron tubes and taking pictures through the transparent tubes at each centimeter level below the surface (Figure 1.1). By collecting these images on tape, and then transferring to a computer, these modern minirhizotron systems have greatly facilitated root research. Because root distributions are often spatially quite variable, particularly in well-structured soils, and the minirhizotron image just represents a small cross-section through the soil, a fairly large number of images may be required to assure statistical significance of results. However, the amount of time required by the previously developed manual procedures for measuring root dimensions in these images is considerable and becomes the main limit of these minirhizotron systems. Therefore, there is a need to work out an efficient and

accurate procedure to automate the extraction and measurement of roots in minirhizotron images. The most difficult part of this task is to automate the extraction of root features in minirhizotron images. Once the roots are extracted, the automated measurement of root dimensions in binary image presents a less difficult task.

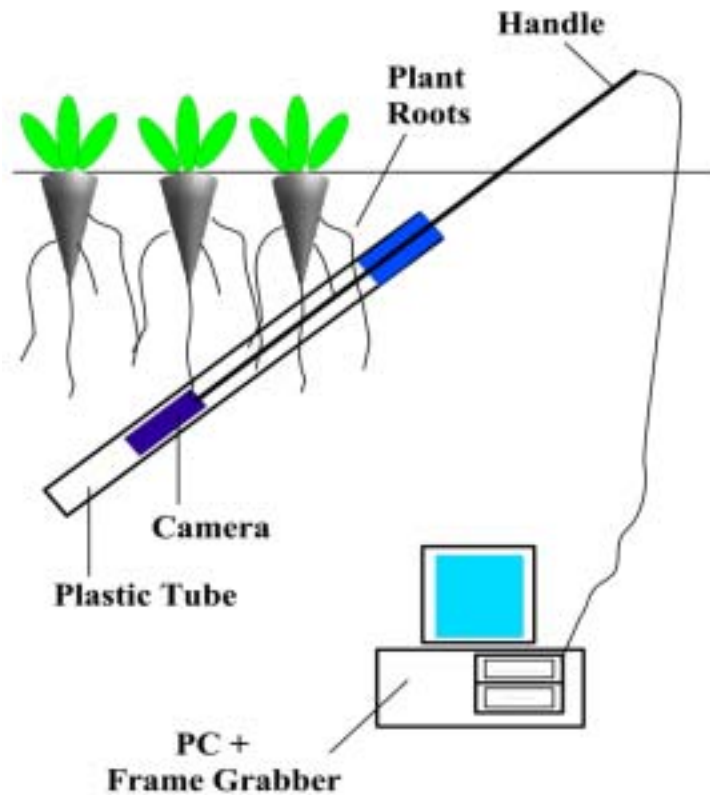


Figure 1.1: An example minirhizotron system

Previous methods to automatically extract roots concentrated on detecting the global intensity distribution or the local intensity gradient in the minirhizotron image, but their standardization has been hampered by quality of the minirhizotron image. Roots are brighter than the background in nearly all portions of the image and exhibit large, local intensity changes. Unfortunately, analysis reveals that other bright extraneous objects that are often found in minirhizotron images also exhibit the same attributes as roots.

1.1 Overview of Approach

In this thesis, we introduce a new approach to detect roots based on their optical and spatial properties. As pointed out by [1], typically, a minirhizotron image is formed of a relatively small area occupied by bright young root and a much larger area by darker background. The basic operation is to enhance the local contrast of bright young roots to the background. Since plant roots share many properties with blood vessels in retinal images, we utilize the two-dimensional matched filter which has been widely used in blood vessel image analysis [2][3][15][23] to enhance individual root segments in the minirhizotron images. Considering the complicated relationship between the foreground and background of the matched filter response (MFR) images, a local entropy thresholding (LET) technique [24] is implemented to extract the enhanced root. In order to avoid shape distortion caused by some mis-enhanced background noise, we apply LET to each corresponding response image from different rotated filters. An area size filter is devised to select root candidates and remove small bright background noise in the thresholded image. A root discrimination method is applied to discriminate roots against the bright extraneous objects from the no-root images by comparing their geometric features. Once the root is identified, we make use of the one-pixel-wide medial axis of the root for length measurement.

1.2 Related Work

Since the manual procedure for locating and measuring roots for a large number of minirhizotron root images is very time-consuming and labor-intensive, current methods are concentrating on automating the procedure for root extraction and discrimination. Most aim at generating a binary image for each minirhizotron image where pixels are labeled either to be on a root or not. As to the root measurement, only a few reports have suggested alternative ways for directly measuring roots in minirhizotron images by hand, most of the

current methods just make use of the automatic length estimators developed for the soil core sampling-based methods.

Because of the existence of some bright background objects in the minirhizotron images, the identification of roots with respect to the background becomes the main problem of automatic minirhizotron images analysis [28]. Since some of these background objects have the same intensity distribution as the roots and the resulting intensity histograms are not the desired bimodal, the global thresholding method [1] applied alone to the minirhizotron images is unable to segment roots accurately.

Vamerali et. al. [28] attempt to acquire the expected bimodal intensity histogram by improving the contrast in the image. An exponential algorithm of contrast stretching is introduced to enhance the local contrast of the root. When the exponential stretching algorithm is completed, the intensity values of most of the background and minor root parts are fell in a narrow range close to 0, while the intensity values of most of the root pixels are converted close to 255, only a few root pixels and some bright background objects are left in the intermediate gray level. However, their global thresholding scheme to extract the enhanced roots is not suitable for large number of minirhizotron root images taken from various backgrounds and recorded with different luminance and exposure levels.

Other methods include a region based seed detection method presented by Erz et. al. [9] and a back propagation artificial neural system (ANS) introduced by Nater et. al. [21]. In [9], a seed is defined as a rather small, distinct part of the root which is clearly identifiable as partial root and has a shape close to a rectangle. Considering each seed region generally has its own optimal threshold, the seed regions are acquired using a dynamic thresholding technique, and then expanded to find the root segment using a contour aligning A* search. Nater et. al. [21] develop an artificial neural system to identify roots in minirhizotron images using the first derivative images produced from the raw images as input, the hand-edited raw image as training image. The back propagation model is trained by repeatedly presenting it with a set of inputs and associated targets response. This system is able to

accurately identify roots in the training images. However, there is a substantial decrease in accuracy when applied to other images on which it had not been trained.

As recently summarized in [29], current methods for reducing no-root objects (i.e., false positives) are based on comparing their geometric features. In [6][20], the length-to-diameter ratio is mentioned to be a suitable parameter for root discrimination. Only object with a length-to-diameter ratio larger than the threshold value will be regarded as root. But the length-to-diameter ratio is only suitable for limited types of root. In [29], roots are discriminated from the bright extraneous objects by detecting another geometric parameter, *elongation index*, which is defined as the square of the perimeter divided by the area. An object with high value of elongation index is classified as a root. In [28], a minimum root length (MLR) method is implemented based on the assumption that the skeletons of those bright background objects are shorter than the experimentally determined MRL. However, this MRL method can not completely detect all the bright background objects, and some short root segments may be eliminated by the MRL filter. In [9], a seed criterion based on shape property, such as width, length, area size and curvature energy, is set for seed selection and these criteria also can distinguish seeds from some bright background objects.

Accurate root measurements are important for improving our understanding of root dynamics and associated functions in plant growth. Various alternative techniques have been devised for estimating root length in minirhizotron images. Most of them are based on two main approaches: (1) manual tracing, and (2) object skeletonization. Manual tracing-based methods measure root length and diameter in digital images by manually tracing of roots on transparent sheets overlain on the TV screen [4] or by applying an interactive procedure, drawing individual roots manually with a PC mouse [13][25]. These methods increase precision, but they are tedious and often require more time than the traditional methods of measuring roots manually. Object skeletonization-based methods estimate the root length as the length of the one-pixel-wide medial line of the object. The simplest method to calculate the medial line length is to count the total number of pixels on the medial line and

multiply by a factor for calibration [11]. Freeman [10] estimated the medial axis length by a chain code length. This length is the sum of the distance between adjacent pixels: the distance between any horizontally or vertically adjacent pairs is 1 and the distance between any diagonally adjacent pairs is $\sqrt{2}$. Since this calculation overestimates the length in most cases, corrections such as calibration using a root of known length as reference [18] or multiplication by an appropriately chosen factor [6][17] have been used. Dorst et. al. [6] used the Pythagorean theorem to calculate root length by rearranging the number of diagonally and orthogonally connected pixels of a line as two legs of a right triangle and estimating the root length as the hypotenuse of the right triangle. The weakness of these methods mentioned above is that lengths are estimated under the assumption that roots are oriented randomly. This assumption is known to cause biased results due to object orientation.

1.3 Thesis Statement

In this thesis, we describe a fully automatic approach to detect and measure roots for large numbers of minirhizotron images. We report our results on minirhizotron images containing a variety of types and sizes of roots, as well as on images containing no roots but some extraneous objects that could be confused with roots. Unlike the edge-tracing algorithm where only root edges are detected, our method can extract the root as a whole. Compared with the previous methods which use the one-dimensional histogram-based thresholding method to extract the enhanced root, our local entropy thresholding (LET) scheme takes into account the spatial distribution of gray levels and the relationship of grayscale statistics of the adjacent pixels in the image. According to our experiment, applying the traditional matched filtering-based methods [2][3][23] to extract roots in the noisy minirhizotron images will result in severe shape distortion, our root extracting scheme can lessen the distortion by applying LET to each corresponding response image from different rotated filters. Our root discrimination methods discriminate roots against bright background

objects by detecting the global geometric features of the object and their intensity distribution properties in the image that are not affected by root type and root length. Compared with other object skeletonized-based root measurement methods, we use the more robust Dijkstra's algorithm to detect the medial line of the root. Compared with the chain code length-based and the Pythagorean theorem-based root length estimator, our length estimator can significantly minimize bias caused by root orientation.

1.4 Thesis Organization

The rest of the thesis is organized as follows. In [chapter 2](#), we explain in more detail about our approach of root extraction and measurement. The introduction of our approach ends with a presentation of a set of methods for discriminating roots against no-root objects in [chapter 3](#). Some results of applying this approach to minirhizotron images are given in [chapter 4](#). Finally, conclusions and future work are presented in [chapter 5](#).

Chapter 2

Approach

Our approach consists of five steps: preprocessing, matched filtering, local entropy thresholding, root selecting and root measuring. The preprocessing step linearly stretches the dynamic range of the gray levels, and then smoothes the images to reduce noise. The matched filtering step enhances the local contrast of the roots based on their optical and spatial properties, and then the enhanced roots are extracted by an entropy-based thresholding scheme in the following step. The root selecting step removes the misclassified pixels in the root image by calculating the area size of each connected group of candidate pixels to determine whether it meets the criteria of a root. The root measuring step uses an accurate method to estimate the root morphology parameters after finding the one-pixel wide medial axis from the skeletonized roots. A schematic diagram of the algorithm is presented in [Figure 2.1](#).

2.1 Preprocessing

The preprocessing step is composed of three phases: grayscale image creating, contrast stretching and image smoothing.

The original image available from video digitizer with a size of 640×480 has three color components: red, green and blue. As shown in [Figure 2.2](#), the green band gives the highest contrast and contains the most detail of a root.

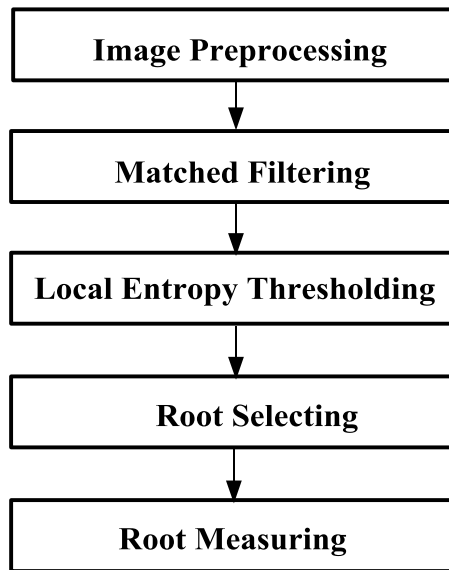


Figure 2.1: The schematic diagram of the algorithm

A linear contrast stretching technique [12] is applied to enhance the intensity contrast of the image. The linear contrast stretch equation is in the following form:

$$J(i,j) = \begin{cases} 0, & \text{if } I(i,j) \leq r_1 \\ I(i,j) \times \frac{r_2-r_1}{255}, & \text{if } r_1 < I(i,j) < r_2 \\ 255, & \text{if } I(i,j) \geq r_2 \end{cases} \quad (2.1)$$

This equation maps the values in intensity image I to new values in J , such that values between r_1 and r_2 in I map to values between 0 and 255 in J . Values below r_1 and above r_2 are clipped; that is, values below r_1 map to 0, and those above r_2 map to 255. For all the experiments, we set r_1 to 153 and r_2 to 204, since most of the young living roots are white and their grayscale intensity values are located in this area.

Finally, in order to reduce background noise such as light soil particles, water droplets and the intensity gradient produced by non-uniform lighting, a 9×9 median filter and a 9×9 mean filter is applied to smooth the image. A root image and its preprocessing results are shown in [Figure 2.3](#).

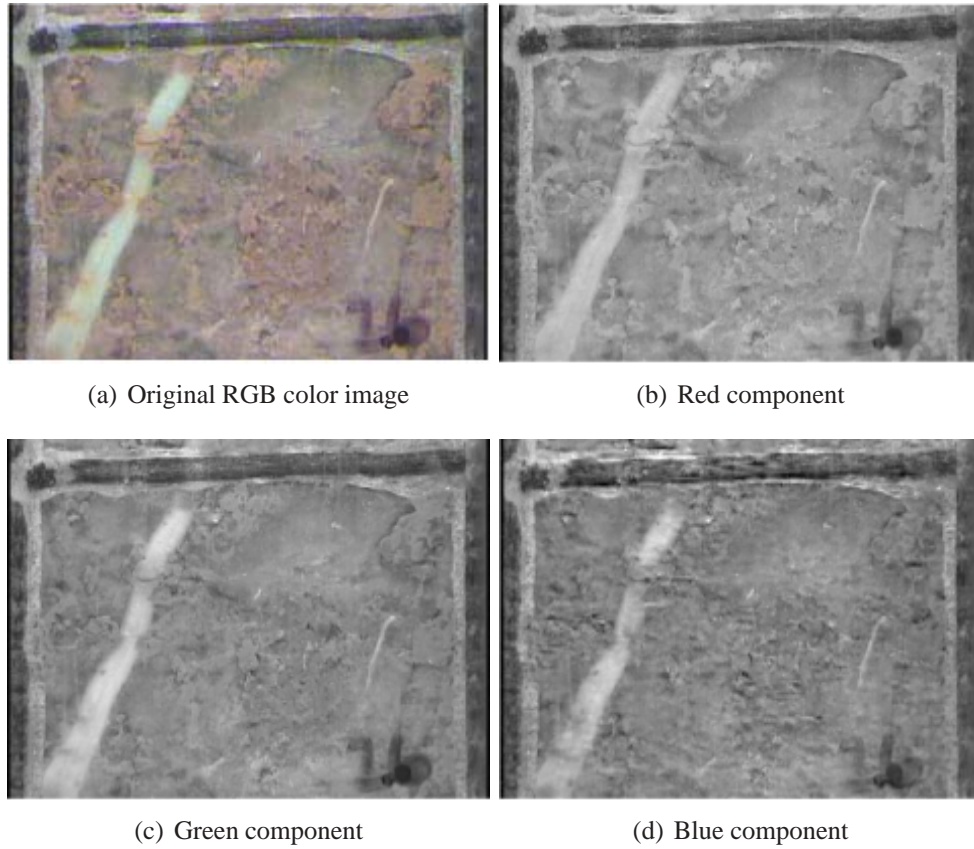


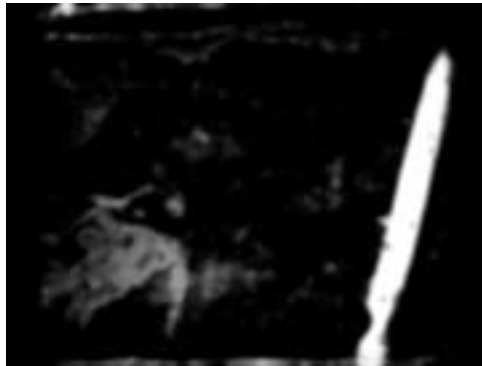
Figure 2.2: RGB color image and its three components in grayscale



(a)



(b)



(c)

Figure 2.3: A root image and its preprocessing result: (a) The original RGB color image. (b) The green component of image. (c) The preprocessed image.

2.2 Matched Filtering

Because a root usually has slight curvatures and the two edges of a root usually run parallel to each other, a root can be represented by piecewise linear directed segments with finite width. Meanwhile, as shown in Figure 2.4, because the young roots appear brighter relative to the background, the gray level profile of the cross section of a young root can be approximated by a Gaussian curve:

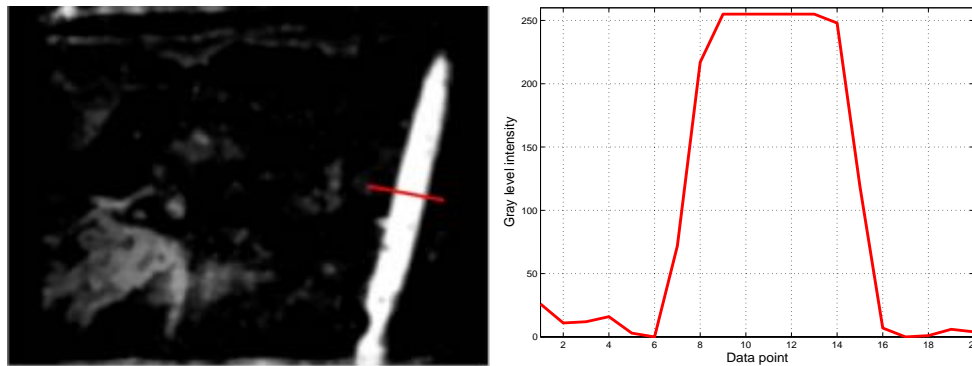


Figure 2.4: A cross section of the root in the preprocessed image (left) and its gray level intensity profile (right)

$$f(x, y) = A \left(1 + ke^{-\frac{d^2}{2\sigma^2}} \right) \quad (2.2)$$

where d is the perpendicular distance between the point (x, y) and the medial axis of the root, σ defines the spread of the intensity profile, A is the gray level intensity of the local background, and k is the measure of reflectance of the plant root relative to its neighborhood.

Considering the properties of roots are very similar to that of the blood vessels, the two-dimensional matched filter kernel developed in [3] for blood vessels is adopted to convolve with the preprocessed image for enhancing the local contrast of the root. Assuming a root has similar cross sections along its length, a number of cross sections are matched simultaneously by convolving with the following kernels:

$$K(x, y) = e^{-\frac{d^2}{2\sigma^2}} \text{ for } |y| \leq \frac{L}{2} \quad (2.3)$$

where L is the length of the segment for which the root is assumed to have a fixed orientation. L and σ are determined experimentally by analyzing roots with different length and diameters. In our systems, we choose $L = 10$ and $\sigma = 2$, such that $K = \{(x, y) \mid |x| \leq 20\sigma, |y| \leq \frac{L}{2}\}$. A sample kernel along 180° is shown in [Figure 2.5](#).

Because of the need to detect vessels of different spatial orientation, the kernel has to be rotated accordingly. We use an angular resolution of 15° , leading to 12 different kernels to span all possible orientations. To detect root segment larger than the matched filter kernel size, the input image is reduced to half size by subsampling, and a set of twelve 81×81 pixel kernels is applied at each size. Four matched filter kernels along 75° , 90° , 135° , 180° and the results of applying them to the preprocessed image given in [Figure 2.3](#) are shown in [Figure 2.6](#). Here, the 135° and 180° kernels are approximately perpendicular to the root segment and find their peak response, while the 75° and 90° kernels get much lower response because they lie nearly parallel to the root segment.

2.3 Local Entropy Thresholding

In order to properly extract the enhanced segments in the matched filter response (MFR) images, an effective thresholding scheme is necessary. Because some MFR images have complicated relationships or overlap between foreground and background, the local entropy thresholding technique is implemented.

For object-background classification of different images with identical histograms ([Figure 2.7](#)), the thresholding techniques based on one-dimensional histograms will result in the same threshold value. In contrast, the local entropy thresholding technique will take the spatial distribution of gray levels into account and threshold them according to their different entropy.

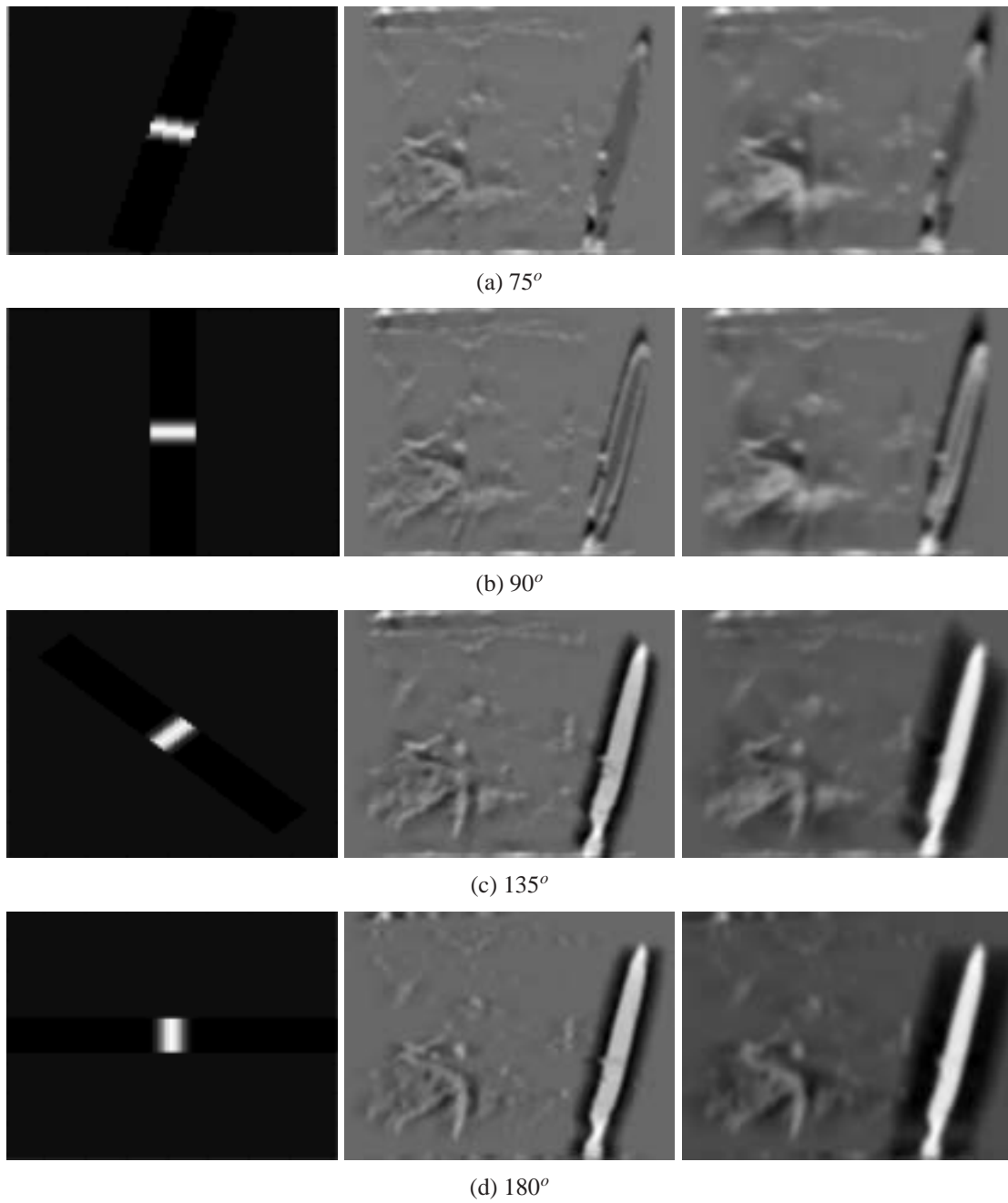


Figure 2.6: Four matched filter kernels and their application results. Left column: The matched filter kernel; Middle column: The full size MFR image; Right column: The half size MFR image. (Scaled for display)

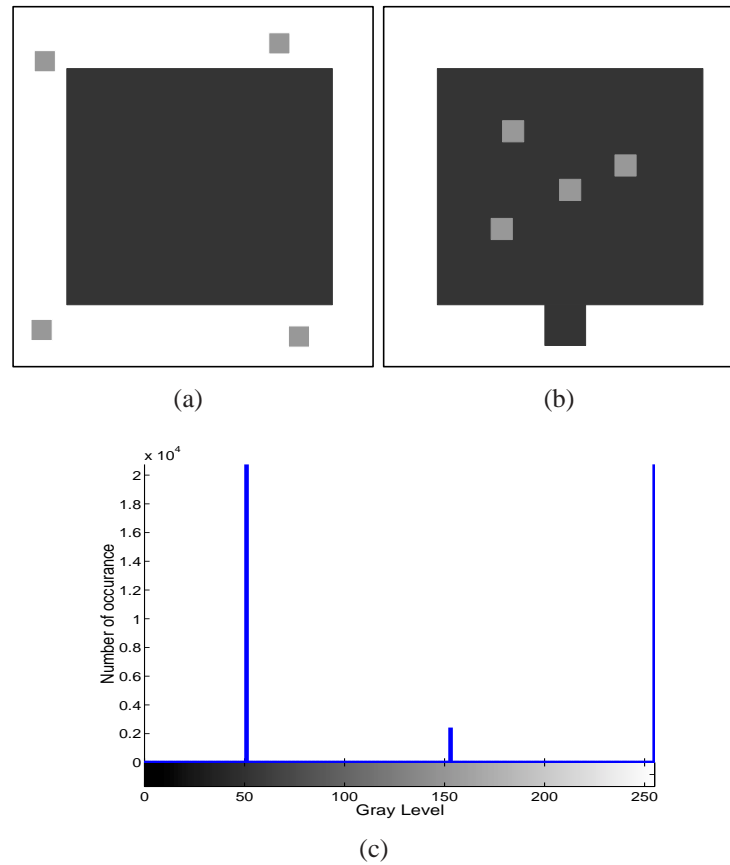


Figure 2.7: Top row: Two different images with the same histogram. The gray levels of the pixels are 51, 153 and 255 respectively in the center square, the four small squares and the outer border. Bottom row: The gray level histogram.

The local entropy thresholding method is based on Shannon's classic notion of entropy [27] and utilizes the elements of the co-occurrence matrix. The concept of Shannon's entropy is the central role of information theory, and it quantifies the bias of a probability distribution. Shannon defined the entropy of an n -state system as:

$$H = \sum_{i=1}^n p_i \log(p_i) \quad (2.4)$$

where p_i is the probability of the occurrence of the event i and

$$\sum_{i=1}^n p_i = 1, \quad 0 \leq p \leq 1 \quad (2.5)$$

For an image F of size $M \times N$, the co-occurrence matrix T of the image gives an idea about the transition of intensities between adjacent pixels, indicating spatial structural information of an image. Depending upon the ways in which the gray level i follows gray level j , slightly different definitions of the co-occurrence matrix are possible. Here, we make the co-occurrence matrix asymmetric by considering the horizontally right and vertically lower transitions. Thus, the element of the $(i, j)^{th}$ entry of the co-occurrence matrix is defined as

$$t_{ij} = \sum_{l=1}^M \sum_{k=1}^N \delta(l, k) \quad (2.6)$$

where

$$\delta(l, k) = \begin{cases} 1, & \text{if } f(l, k) = i \text{ and} \\ & f(l, k+1) = j \\ & \text{or} \\ & \text{if } f(l, k) = i \text{ and} \\ & f(l+1, k) = j \\ 0, & \text{otherwise} \end{cases} \quad (2.7)$$

Figure 2.8 shows a simple example of the co-occurrence matrix of a 3×3 image with 4 gray levels (0, 1, 2 and 3).

1	2	3	0	0	0	0
1	2	3	0	2	3	0
1	2	3	0	0	0	2
	(a)			(b)		

Figure 2.8: A 3×3 matrix (left) and its co-occurrence matrix (right).

Therefore, the two-dimensional histogram of an image can be written as

$$P_{ij} = \frac{t_{ij}}{\sum_{i=0}^G \sum_{j=0}^G t_{ij}} \quad (2.8)$$

It actually is a two-dimensional representation of the probability of grayscale level transitions in an image. [Figure 2.9](#) demonstrates that although the two images in [Figure 2.7](#) have the same one-dimensional histogram, their two-dimensional histograms are different.

If we selecting s ($0 \leq s \leq G$, G is the maximum grayscale value 255) to be the threshold then the co-occurrence matrix is partitioned into four quadrants, namely A, B, C, and D as shown in [Figure 2.10](#). These correspond respectively to the transition from background-to-background, background- to-foreground, foreground-to-background, and foreground-to-foreground. The local entropy is defined by the quadrants A and D.

The probabilities of a pixel being in quadrant A and D can be defined as

$$P_A = \sum_{i=0}^s \sum_{j=0}^s p_{ij} \quad (2.9)$$

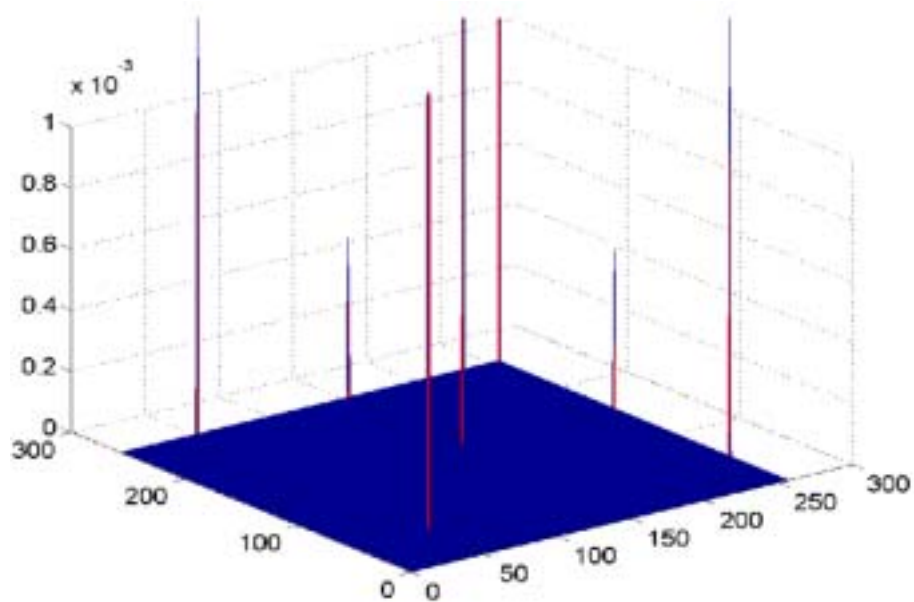
$$P_D = \sum_{i=s+1}^G \sum_{j=s+1}^G p_{ij} \quad (2.10)$$

The probability of an $i \rightarrow j$ transition can be normalized by dividing by the probability of being in the $i \rightarrow j$ quadrant,

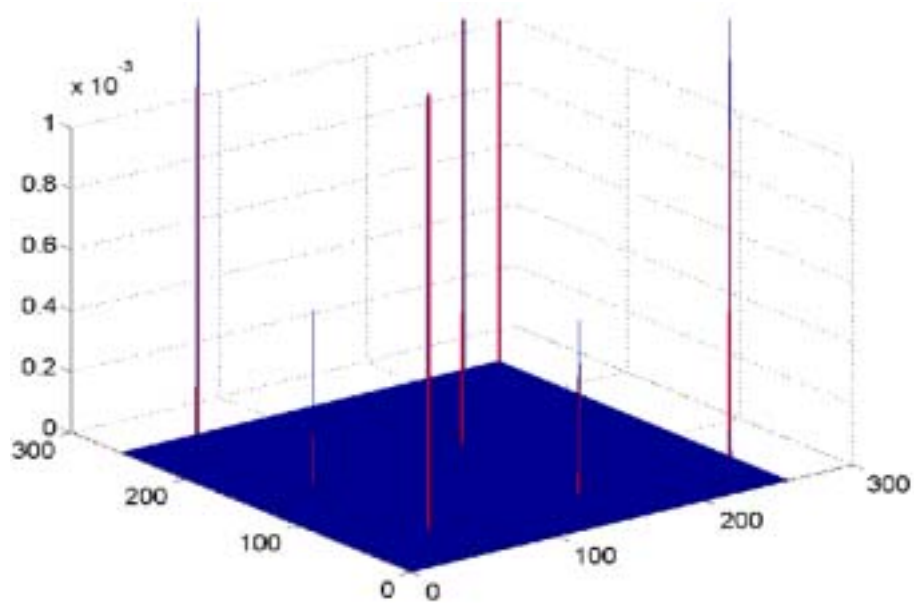
$$P_{ij}^A = \frac{p_{ij}}{P_A} = \frac{t_{ij}}{\sum_{i=0}^s \sum_{j=0}^s t_{ij}} \quad (2.11)$$

$$P_{ij}^D = \frac{p_{ij}}{P_D} = \frac{t_{ij}}{\sum_{i=s+1}^G \sum_{j=s+1}^G t_{ij}} \quad (2.12)$$

The resulting probabilities are called the transition probability distribution. The local entropy method uses the spatial correlation in the image as the criterion for selecting the optimal threshold, by attempting to maximize the probability that similar pixels are grouped together. It is based on the probability distribution for foreground-to-foreground and background-to-background transitions in the co-occurrence matrix.



(a) The 2D histogram of Figure 2.7(a)



(b) The 2D histogram of Figure 2.7(b)

Figure 2.9: The 2D histogram of the two images in Figure 2.7.

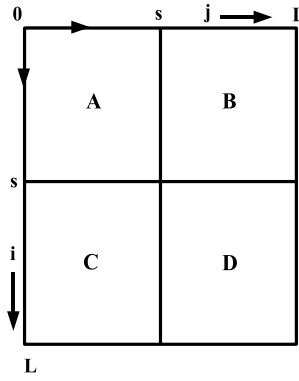


Figure 2.10: Quadrants of the co-occurrence matrix

Background-to-background entropy:

$$H_A(s) = -\frac{1}{2} \sum_{i=0}^s \sum_{j=0}^s P_{ij}^A \log P_{ij}^A \quad (2.13)$$

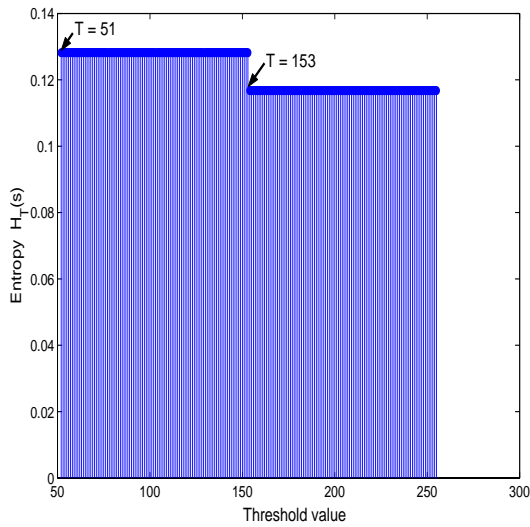
Foreground-to-foreground entropy:

$$H_D(s) = -\frac{1}{2} \sum_{i=s+1}^G \sum_{j=s+1}^G P_{ij}^D \log P_{ij}^D \quad (2.14)$$

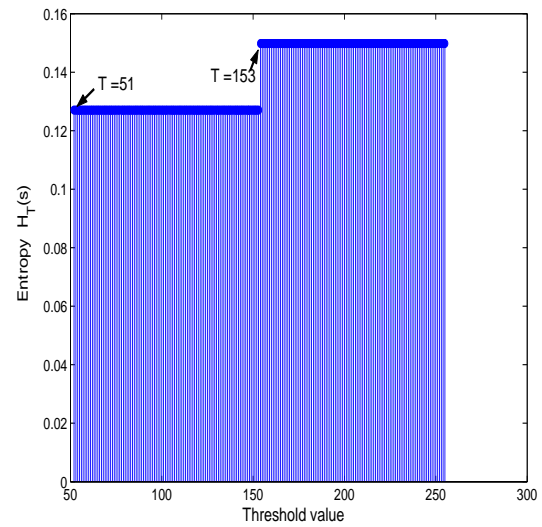
$$H_T(s) = H_A(s) + H_D(s) \quad (2.15)$$

The components of $H_T(s)$ measure the relative probability of transitions from background-to-background or foreground-to-foreground, so maximizing the local entropy will favor thresholds that group similar grayscale values together. As shown in [Figure 2.11](#), the gray level corresponding to the maximum of $H_T(s)$ gives the optimal threshold for object-background classification of the images in [Figure 2.7](#). The results of applying the local entropy thresholding to the matched filtering response (MFR) images given in [Figure 2.6](#) are shown in [Figure 2.12](#).

The previous method described in [2] constructed a combined matched filter response (MFR) image by comparing each of the corresponding MFR images from the 12 different rotated filter pixel-by-pixel and choosing the one with the maximum response value, and



(a) Entropy thresholding curve of Figure 2.7(a)



(b) Entropy thresholding curve of Figure 2.7(b)

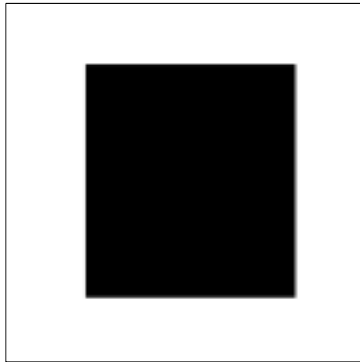
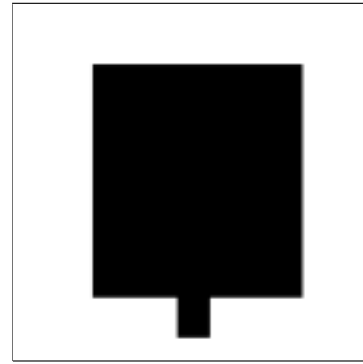
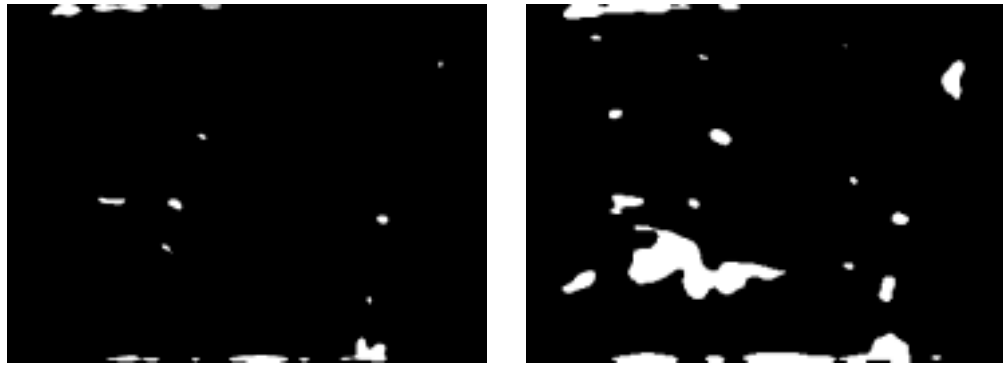
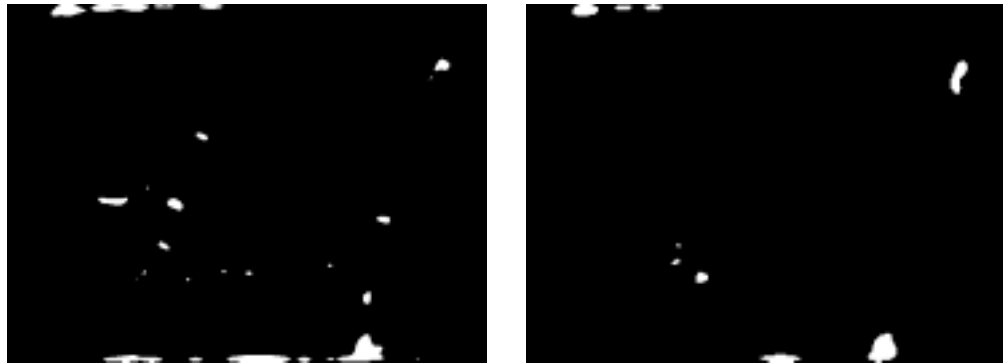
(c) Entropy thresholded image of Figure 2.7(a), $T=51$ (d) Entropy thresholded image of Figure 2.7(b), $T=153$

Figure 2.11: Selecting the optimal threshold for object-background classification of the two images in Figure 2.7.

then applied thresholding to extract the enhanced objects from the combined MFR image. However, we find that using this scheme to extract the enhanced roots in our experiments will result in shape distortion, because some bright background noises close to the main root segment are misclassified and finally mixed with the main root after thresholding. Considering some of these bright background noise are actually enhanced with their adjacent main root by different kernels, without firstly combining the separate MFR images from different rotated filter, we directly apply the local entropy thresholding to each of the



(a) The thresholded images of Figure. 2.6(a)



(b) The thresholded images of Figure. 2.6(b)



(c) The thresholded images of Figure. 2.6(c)



(d) The thresholded images of Figure. 2.6(d)

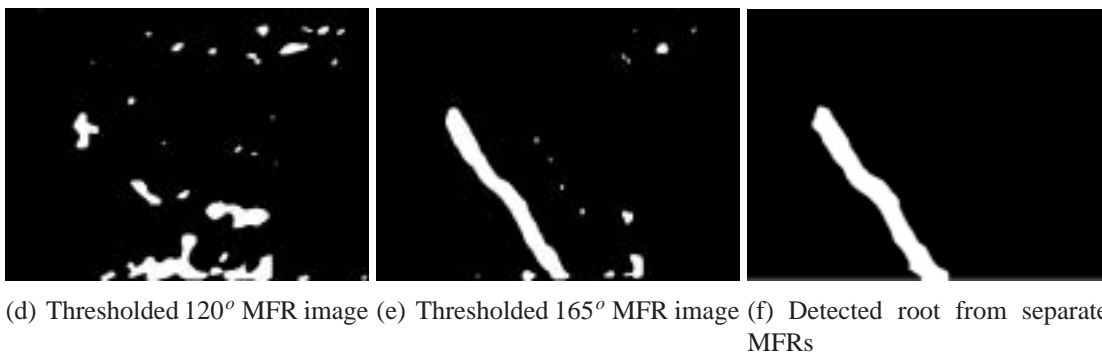
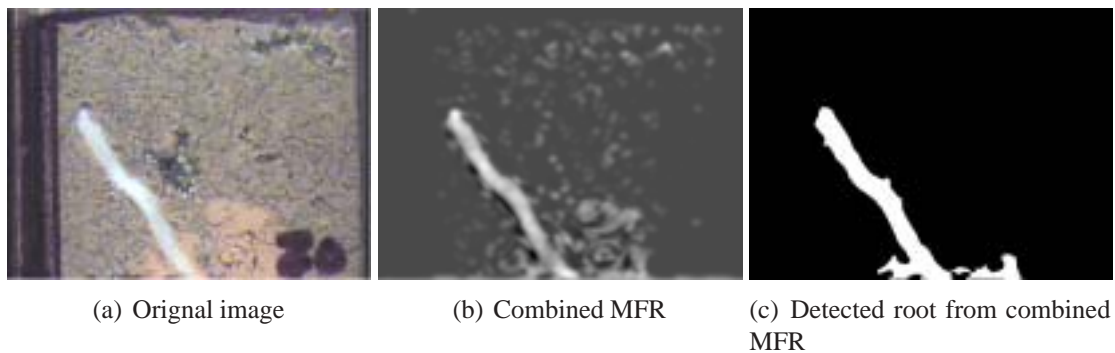
Figure 2.12: The corresponding LET output of the MFR images in Figure. 2.6.

MFR image to extract the enhanced bright objects. As shown in [Figure 2.13](#), we can find that those misclassified bright background noise which will cause the shape distortion in the previous method and their adjacent main root are thresholded to different binary images and will be isolated and finally discarded in next root selecting step.

2.4 Root Selecting

Now that we have a set of binary images, we need to find out the roots in these images. To do this, we adopt the straightforward approach of extracting the largest object in each thresholded image. Of course, this relies upon the simplifying assumption that there is exactly one root per image, which, when applied to a no-root image will false detect a no-root object. In the next chapter, we will discuss ways of enabling the algorithm to also work when there is no root present.

Connected component labeling is a simple image analysis technique that scans an image pixel-by-pixel and groups its pixels into components based on pixel connectivity. Here, we use this technique to identify individual objects in each thresholded image. Considering that the area size of the root segment region is much larger than that of most bright background objects, only the largest component in each thresholded image is selected as the root candidate and stored in candidate group P . We assume that the peak responses of any root segment at different rotated kernels should have approximately the same area, so among all the candidates in P , only the candidate P_i with an area size $A_i \geq 0.8A_{max}$ will be regarded as the peak matched filter response of the detected root. As shown in [Figure 2.14](#), 24 objects are selected as the root candidates from each thresholded image, some of which are bright background noise rather than actual roots. After applying the area size filtering ($A_i \geq 13456$), only the candidates highlighted in bold in [Table 2.1](#) will remain. Once the previous phases are completed, an entire root is acquired by combining all the remained



Another example:

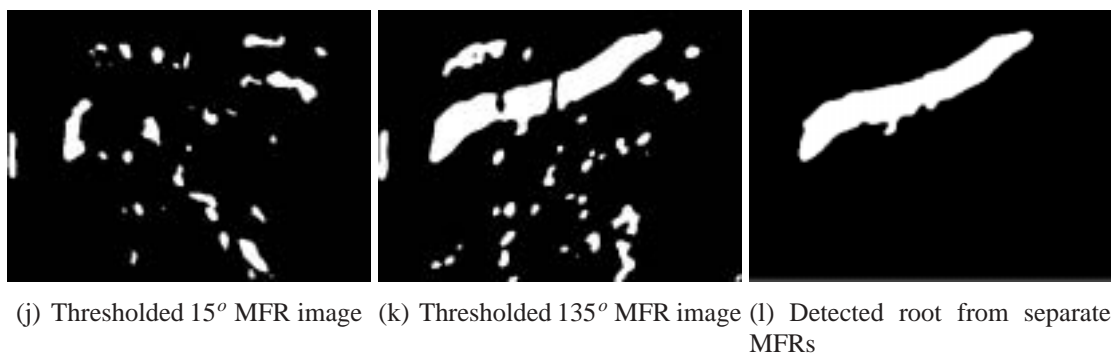
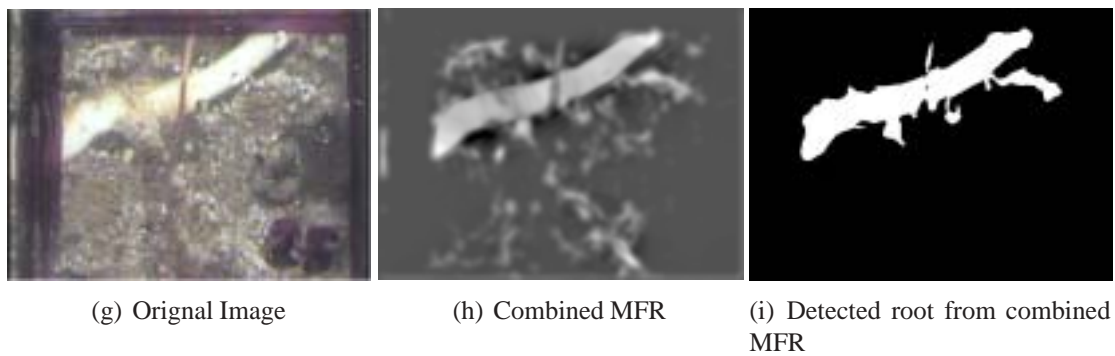
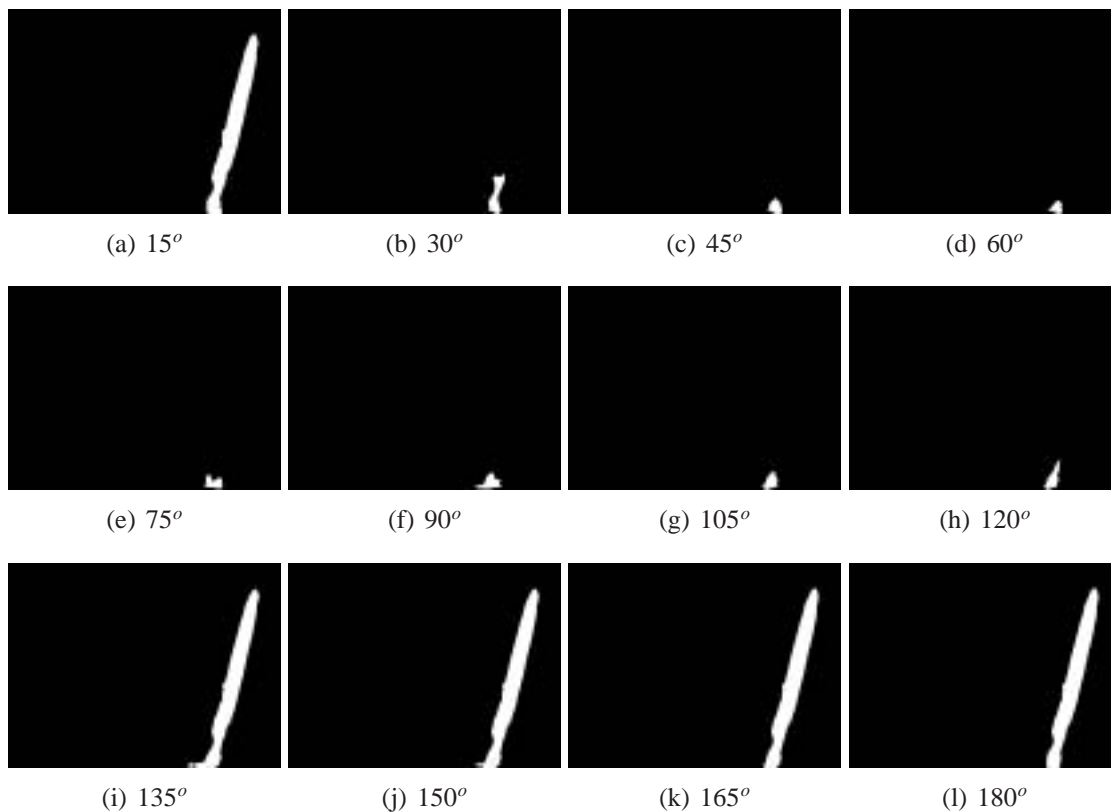


Figure 2.13: A comparison between the LET outputs of these two different schemes.

Full size images:



Half size images:

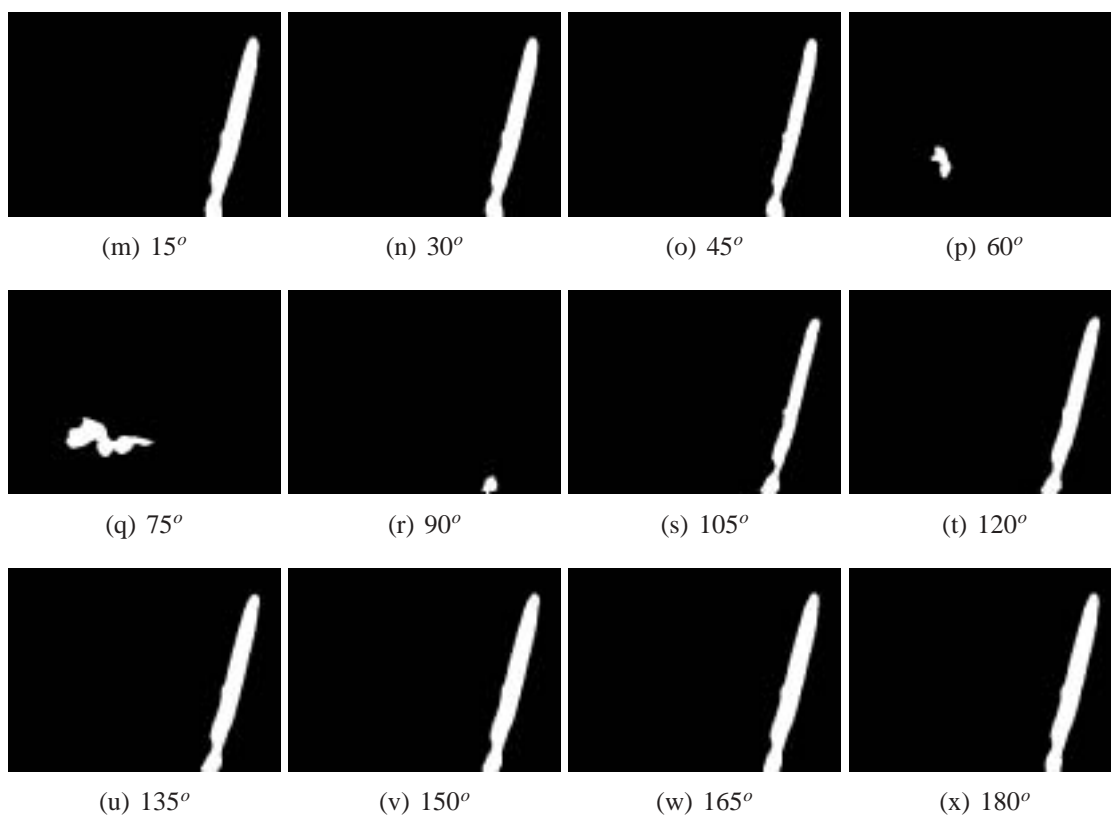


Figure 2.14: The root candidates selected from the thresholded images in Fig. 2.7;

Orientation	Area (Full size image)	Area (Half size image)
15°	14198	16688
30°	1752	15880
45°	740	13564
60°	559	1796
75°	861	7908
90°	1059	980
105°	879	12504
120°	1129	15040
135°	14124	16136
150°	14275	16604
165°	14523	16820
180°	14417	16692

Table 2.1: Root candidate selecting from Figure. 2.14. Here the area size filter is 13456.

candidates together using the logical operator OR (Figure 2.15). This root selecting method can efficiently eliminate the smaller bright background noise in the root images.



Figure 2.15: The output of root selecting

2.5 Root Measuring

Our method of root measurement is based on object skeletonization. To measure the root length, firstly we need to find the medial line of the root. For a root with smooth shape, its medial axis can be represented by the one-pixel-wide skeleton acquired by applying the morphological technique known as “thinning” (Figure 2.16). However, for a root with

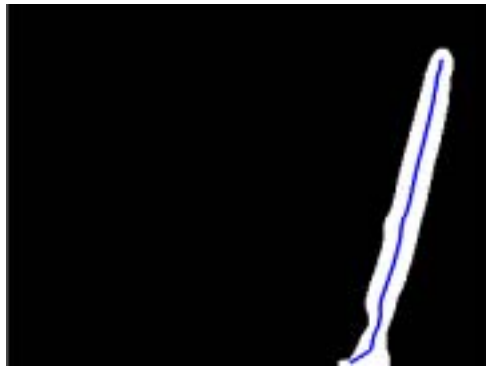


Figure 2.16: The one-pixel-wide skeleton of a smooth root

slight irregularity in the shape, its final skeleton will have some short branches, which we called *skeleton tree* (Figure 2.17(a)). In order to extract the medial axis from the skeleton tree, we apply the widely used shortest paths finding technique *Dijkstra's algorithm*. If each pixel on the skeleton tree represents a node on a graph, the connection between two adjacent pixels represents an edge of the graph and the Euclidean distances between these two adjacent pixels represent edge weights, then the medial axis of the root can be represented by the found shortest path from the first node to last node on the graph with lowest distance cost (Figure 2.17(b)).

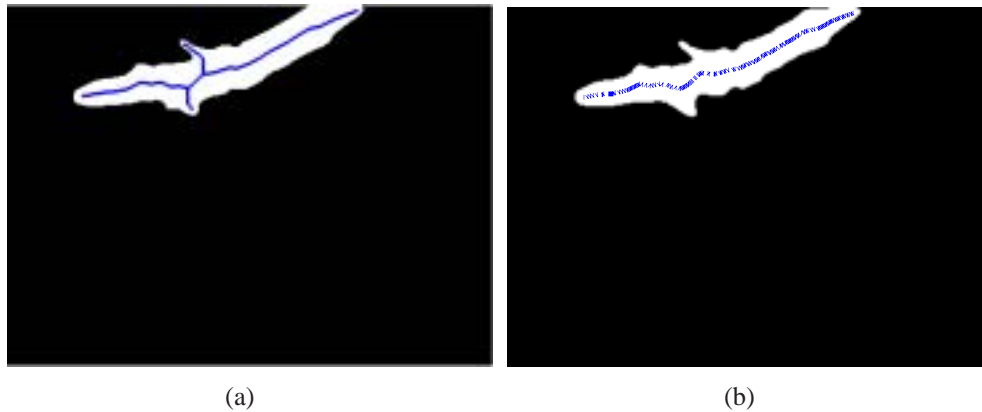


Figure 2.17: An example of finding medial axis of root from its skeleton tree. (a) The skeleton tree of a root caused by slight irregularities in the shape, (b) The found medial axis from the skeleton tree using Dijkstra's algorithm.

After extracting the medial axis using Dijkstra's algorithm, the nodes on the medial axis are sequentially stored in the set C . We can easily count the number of orthogonally connected nodes pair N_o and diagonally connected nodes pair N_d on a medial axis by calculating their distance (Figure 2.18(a)). For any two consecutive nodes C_i and C_j in C , if their distance $D_{ij} = \sqrt{2}$, this is a diagonal connection pair and $N_d = N_d + 1$; if $D_{ij} = 1$, this is an orthogonal connection pair and $N_o = N_o + 1$. Freeman formula [10] estimates the length of the medial axis as the sum of the distance of consecutive nodes, and the equation is:

$$L = \sqrt{2}N_d + N_o \quad (2.16)$$

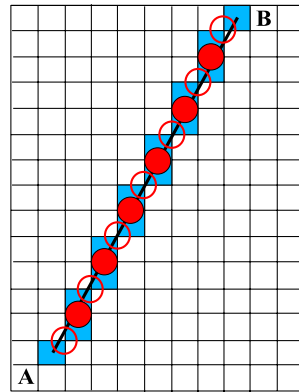
However, because the roots are randomly oriented in the minirhizotron image, this method overestimates the root length in most cases (Figure 2.18(b)). If we rearrange these connection circles as Figure 2.18(c), the Pythagorean theorem [6] estimates the root length as the hypotenuse of the right triangle, and the equation is:

$$L = (N_d^2 + (N_o + N_d)^2)^{1/2} \quad (2.17)$$

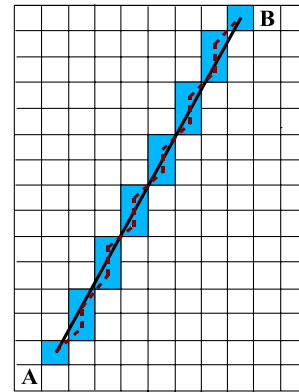
This method is accurate when used to measure single-line medial axis, but will underestimate the multi-line medial axis, such as the example shown in Figure 2.18(d).

In our research, we adopt a more accurate method, called Kimura's length estimator, which can compromise the overestimation and underestimation caused by the Freeman formula and the Pythagorean theorem. We estimate the length of the medial axis AB as the total length of AE and EB (Figure 2.19(a)). For a multi-line medial axis such as the one shown in Figure 2.18(d), the sum of the length of AF and FB will be approximated by the total length of the two virtual lines AE and EB (Figure 2.19(b)), and the Kimura's length estimating equation is:

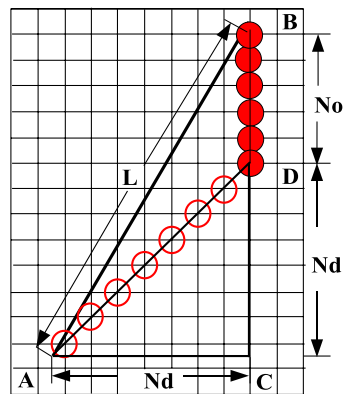
$$L = \left[N_d^2 + (N_d + N_o/2)^2 \right]^{1/2} + N_o/2 \quad (2.18)$$



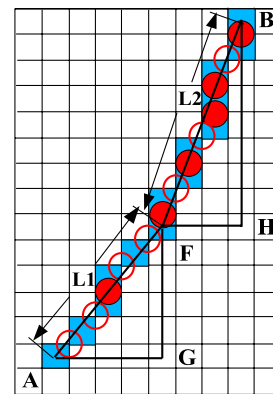
(a)



(b)



(c)



(d)

Figure 2.18: (a) A single line medial axis is represented as meshed pixels. An open circle shows a diagonally connected pair of pixel and a closed circle shows an orthogonally connected pair of pixels. (b) Freeman formula estimates the actual root length as the length of the dash line. (c) The line AB is the oblique side of a right angle triangle ABC. The open and closed circles are arranged that the length of AC is defined as N_d and that of BC is defined as N_d plus N_o . Pythagorean theorem estimates the actual length of the root as the length of AB. (d) A two-line medial axis is represented as meshed pixels. Pythagorean theorem estimates the actual length of the two lines AF and FB as the length of AB, while $AB < AF + FB$.

Making use of the medial axis, we can also easily measure the average diameter of the

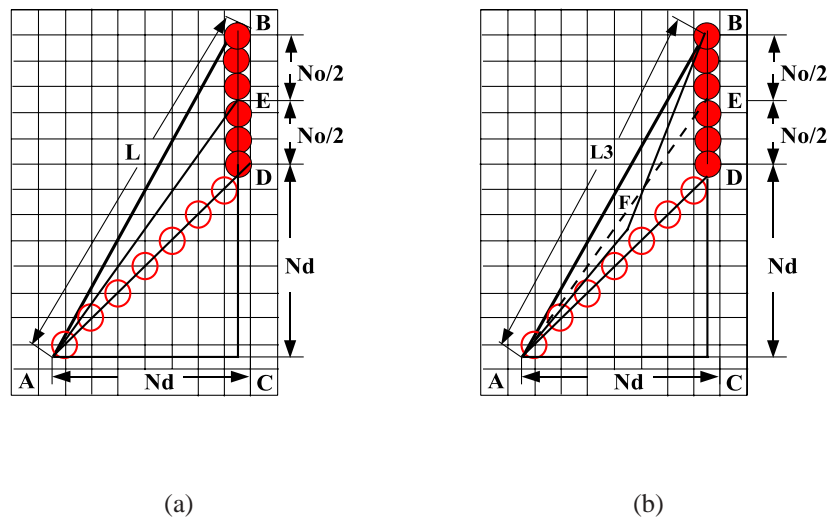


Figure 2.19: (a) Kimura's method estimates the actual length of AB as the length of two lines AE and EB. The length of AE is calculated by applying the Pythagorean theorem to right triangle AEC. (b) Kimura's method estimates the actual length of the two lines AF and FB as the length of the two virtual lines AE and EB.

root. We select 10 nodes on the medial axis that divide the medial axis into 11 equal parts, find their corresponding opposite boundary point pairs, and then calculate the distance between each opposite boundary point pair. Considering some segmented roots have slight shape distortion because of the image quality, we discard the two opposite boundary point pairs with the maximum and the minimum distance and estimate the average diameter of the root as the average distance of the remaining opposite boundary point pairs. An example of root measurement is shown in [Figure 2.20](#).

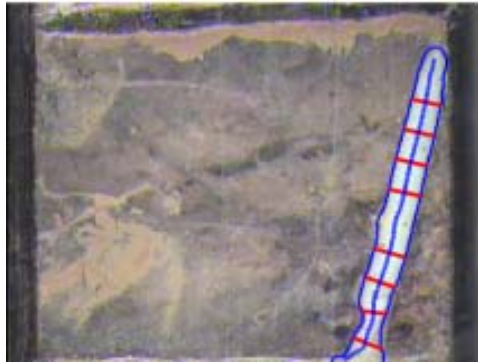


Figure 2.20: An Examples of root measurement.

Chapter 3

Root Discrimination

As mentioned in the previous chapter, our root selecting method can efficiently ignore the bright background objects in the minirhizotron root images. However, when applied to images that do not contain a root, our approach will detect a no-root object. These falsely detected no-root objects may be caused by some bright extraneous object or uneven diffusion of light through the minirhizotron wall (Figure 3.1). In our research, we explore a set of geometric features based on shape description to discriminate roots, (1) eccentricity, (2) approximate line symmetry and (3) boundary parallelism. Two other methods detecting the intensity distribution frequency and discontinuity are also tested: (4) histogram distribution and (5) edge detection. These approaches are described in this chapter and experimentally evaluated in chapter 4.

3.1 Eccentricity

The eccentricity of an ellipse is the ratio of the distance between the foci of the ellipse to its major axis length. For a general 2D shape, its eccentricity can be estimated as that of the ellipse which has the same second-moments as it. The value is between 0 and 1, a 2D shape whose eccentricity is 0 is actually a circle, while a 2D shape whose eccentricity is 1 is a line segment. Since the length of a root is much longer than its width, its eccentricity

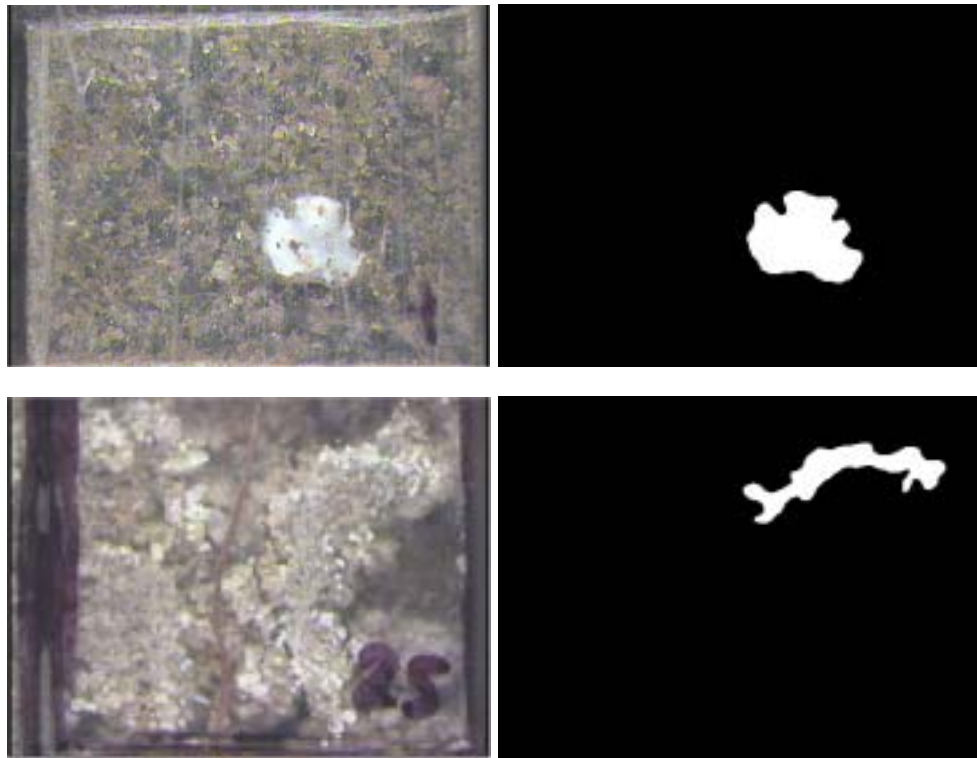


Figure 3.1: Examples of falsely detected root. First row: A falsely detected root caused by a bright extraneous object; Second row: A falsely detected root caused by the uneven diffusion of light through the minirhizotron wall.

is very close to 1, while the shape of no-root object is irregular, causing its eccentricity to be relatively lower. Hence, a properly selected eccentricity value threshold can be used to discriminate roots against no-root objects (Figure 3.2).

3.2 Approximate Line Symmetry

A geometric shape is said to be symmetric with respect to a line if the line bisects all line segments that are perpendicular to the line and terminated by the shape outline, and the line will be called *medial axis*. Because the 2D shape of the root segment approximates an elongated rectangle and has approximate line symmetry with respect to its medial axis, while

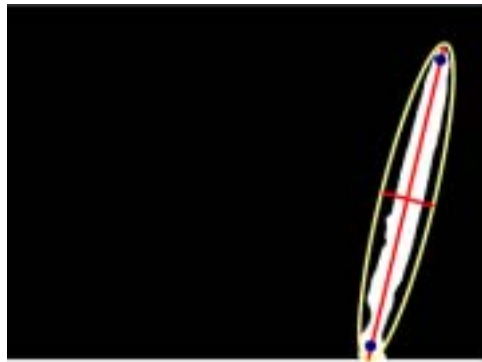


Figure 3.2: An example of discriminating root by detecting its eccentricity

the irregular shape of a no-root object does not exhibit such symmetry (Figure 3.3), we attempt to distinguish roots from no-root objects by detecting if they have line symmetry.

After extracting the medial axis of an object using Dijkstra's algorithm, for each point

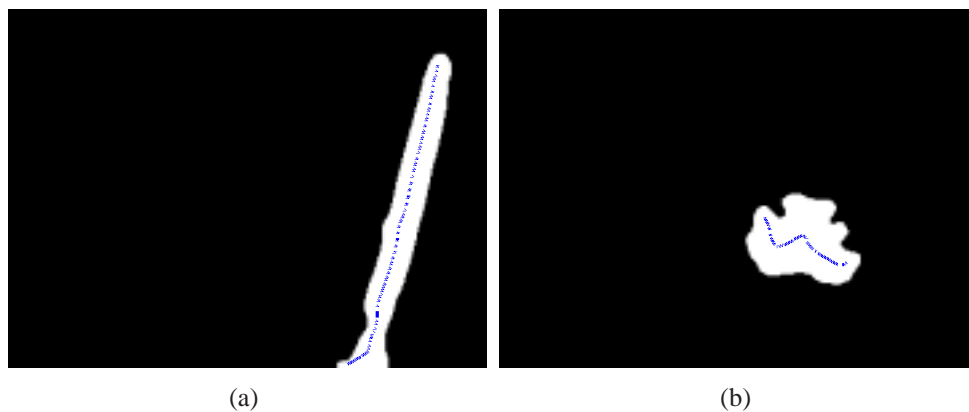


Figure 3.3: An example of classifying an object by detecting its approximate line symmetry. (a) an approximate line symmetrical root; (b) an unsymmetrical no-root object.

C_i on the medial axis C , we search along the line perpendicular to the medial axis at C_i to find the two points where the line intersects the boundary. Then we calculate the ratio of the distance between C_i and the two boundary points. If the ratio is nearly 1 (i.e., the perpendicular line bisects the medial axis), we say that the object is symmetric about the medial axis C at the point C_i . The percentage, M , of points along C that pass the test indicates the line symmetry of the object. Selecting an optimal ratio as the threshold, we can efficiently discriminate roots against no-root objects.

3.3 Boundary Parallelism

The 2D shape of a root segment approximates an elongated rectangle which means that the shape width is approximately constant or varies continuously. After some smoothing, the opposite boundaries of the root segment should be nearly parallel. Based on this assumption, we discriminate a root from a no-root object by detecting the parallelism of the opposite boundaries. Making use of the medial axis, for each point C_i on the medial axis, we find its corresponding opposite boundary point pair whose joining line is perpendicular to the medial axis at C_i as before, and then we compare their slopes computed by Sobel edge detector. If their slopes are similar to each other, we say that the opposite boundaries is parallel to each other at the point C_i . The percentage, P , of points along C that pass the parallel test reflects the parallelism of the opposite boundary of the object. If we can find a precise boundary parallelism threshold, then any objects with a ratio P larger than this threshold value will be classified as a root.

3.4 Histogram Distribution

The histogram of a digital image with gray levels in the range $[0, G]$ is a discrete function $h(r_k) = n_k$, where r_k is the k th gray level and n_k is the number of pixels in the image having gray level r_k [12]. For an 8-bit grayscale image, G is 255. The histogram distribution method is based on two assumptions: (1) In a grayscale image, only the bright objects or areas will be extracted; (2) Among the extracted bright objects, roots are brighter than the no-root objects. An example of the histogram distribution test is shown in [Figure 3.4](#).

In this method, we calculate the intensity histogram of the object, followed by the percentage of pixels in the object with an intensity value between 200 and 255. This percentage, H , reflects the brightness of the detected objects, and is also a good criteria to discriminate roots from no-root objects.

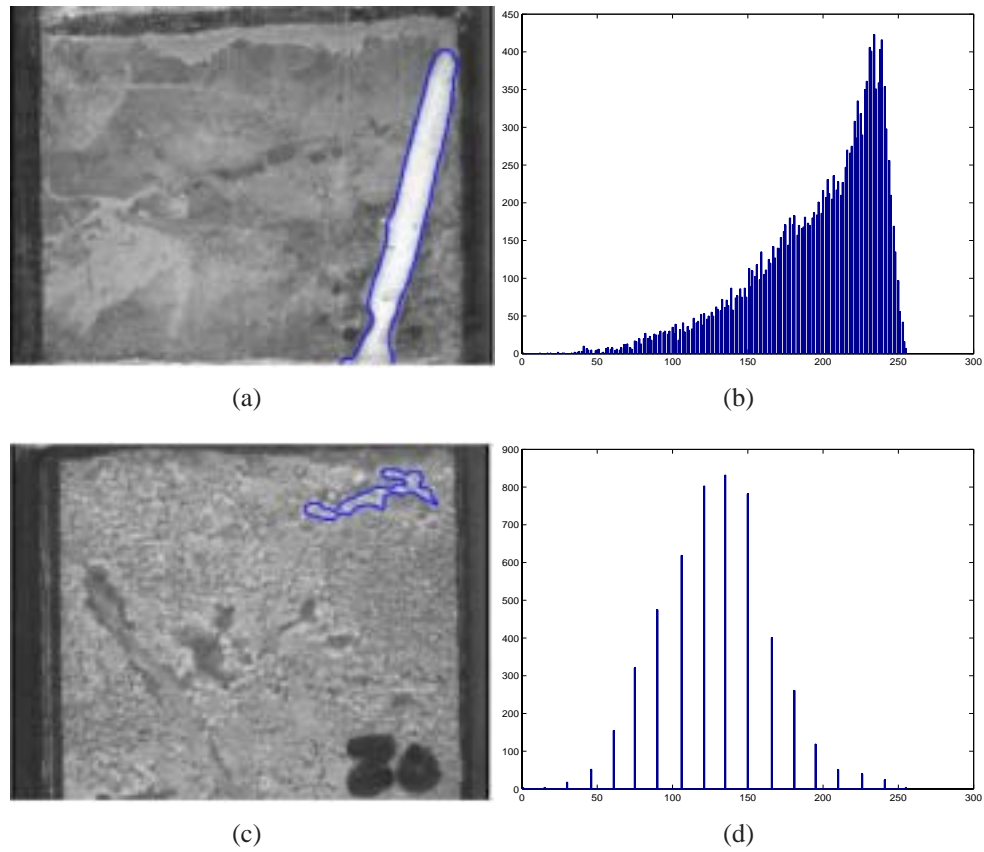


Figure 3.4: An example of histogram distribution method: (a) The outline of a detected root in original grayscale image; (b) The histogram of the root; (c) The outline of a no-root object in original grayscale image; (d) The histogram of the no-root object.

3.5 Edge Detection

Edges are places in the image with strong intensity contrast. The edge detection method is based on the assumption that a smooth root region should have little intensity discontinuity while a no-root object will likely contain significant local intensity changes which will produce considerable edge points (Figure 3.5).

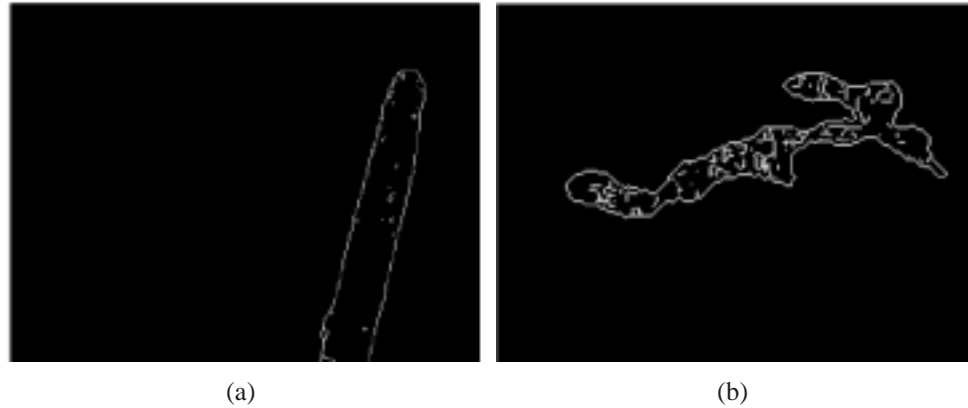


Figure 3.5: An example of edge detection method: (a) The detected edge points inside a root; (b) The detected edge points inside a no-root object.

Since edges correspond to strong intensity contrast, they can be detected using the magnitude of the image. The Sobel operator is a widely used gradient edge operator that convolves the image with two kernels, one estimating the gradient in the x-direction, S_x , the other estimating the gradient in the y-direction, S_y .

$$S_x = \begin{bmatrix} -1 & 0 & 1 \\ -2 & 0 & 2 \\ -1 & 0 & 1 \end{bmatrix}, \quad S_y = \begin{bmatrix} 1 & 2 & 1 \\ 0 & 0 & 0 \\ -1 & -2 & -1 \end{bmatrix} \quad (3.1)$$

The absolute gradient magnitude is then estimated as:

$$|S| = |S_x| + |S_y| \quad (3.2)$$

After having calculated the magnitude of the first derivative, we identify those pixels corresponding to an edge by looking for a local maximum in the gradient image, thus producing one pixel wide edges. The percentage, R , of the amount of no-edge pixels to the pixel amount of the object is calculated. Here, R indicates the smoothness of the object boundary, and can be used as a threshold to classify roots.

3.6 Optimal Threshold Selecting

For each of these five methods, we need to select an optimal threshold value to discriminate roots. Here, we use Receiver Operating Characteristic (ROC) analysis to search the optimal threshold for each method.

The ROC curve is constructed by plotting a series of pairs of true positive rate (TPR) and false positive rate (FPR) calculated by varying the threshold value in a range. TPR rate and FPR rate can be calculated using the following equations:

$$TPR = \frac{\text{number of true positives}}{\text{number of roots in the detected images}} \quad (3.3)$$

$$FPR = \frac{\text{number of false positives}}{\text{number of no-root objects in the detected images}} \quad (3.4)$$

The true positive is the number of correctly detected roots, the false positive is the number of incorrectly detected roots.

Every point on the ROC curve represents a (FPR, TPR) pair created by the threshold value. An optimal threshold value is then chosen as the one that generates a point in the ROC graph closest to (0,1), which represents the perfect classification. The ROC curves of each method and the experimental results of optimal thresholding estimation are shown and discussed in [chapter 4](#).

Chapter 4

Experimental Results

In our research, we tested forty-five 640×480 pixel minirhizotron images; thirty of them are one-root images which contain various types of roots with different size, the remaining fifteen images are no-root images which are composed of only background objects or dead roots. As shown in [Figure 4.1](#), the outputs of our algorithm are compared with hand-labeled ground truth provided by the Clemson Root Biology Lab.

One problem in the proposed scheme is the varying root diameters. In [\[23\]](#), a set of matched filters is constructed with different kernel sizes. For every supposed root diameter, a new kernel has been built with different σ . However, the computation increases linearly with the number of different kernels being added, and the practical experimentations shows that the improvement achieved does not warrant such extra computations. In our research, a subsampling technique is applied to scale the original grayscale image to half size. After constructing the kernels with $\sigma = 2$ and $|x| \leq 20\sigma$, which match well with a root of medium diameter for the minirhizotron images being considered in our research, the matched filters are applied to the images at each size. The results in [Figure 4.1](#) show that our method works well for roots with diameter varying from narrow to wide.

In our research, two automatic thresholding methods are tested and compared: Otsu's thresholding method [\[22\]](#) and local entropy thresholding method. As a one-dimensional

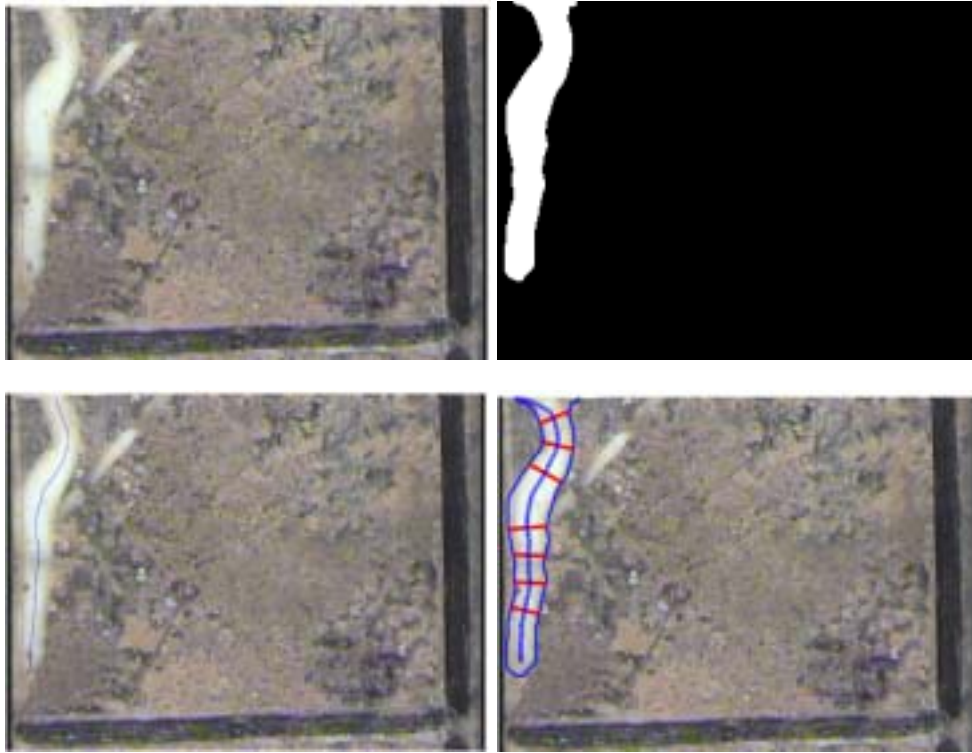


Figure 4.1: The results of applying our approach to 12 sample images. First row: Input Image and Extracted root; Second row: Hand-labeled medial axis and measured root.

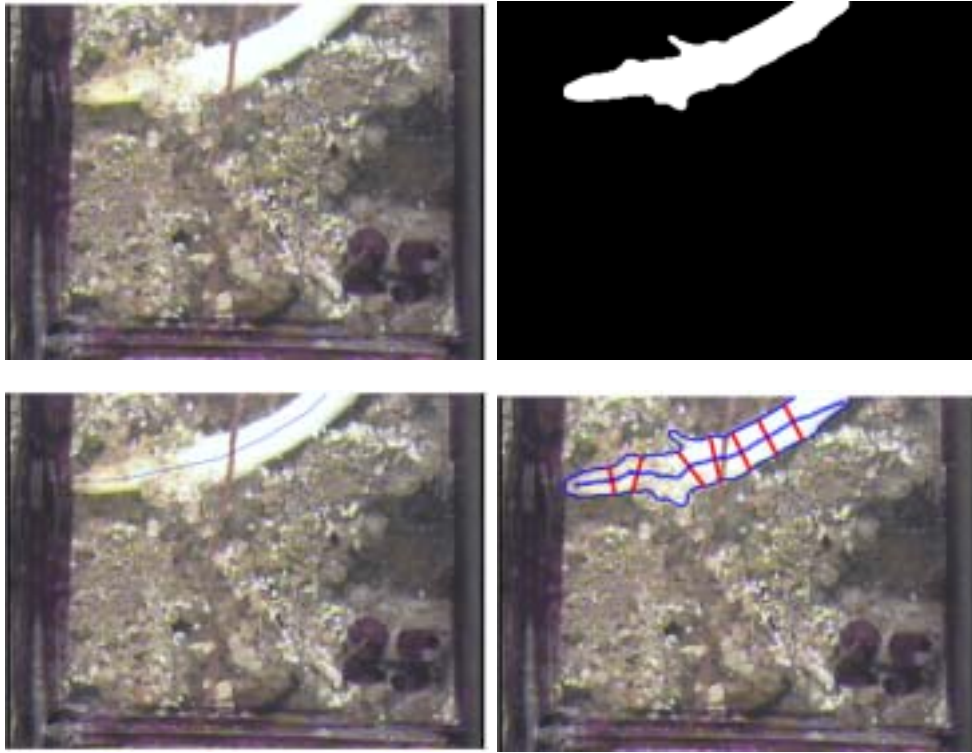


Figure 4.1: The results of applying our approach to 12 sample images. First row: Input Image and Extracted root; Second row: Hand-labeled medial axis and measured root. (cont.)

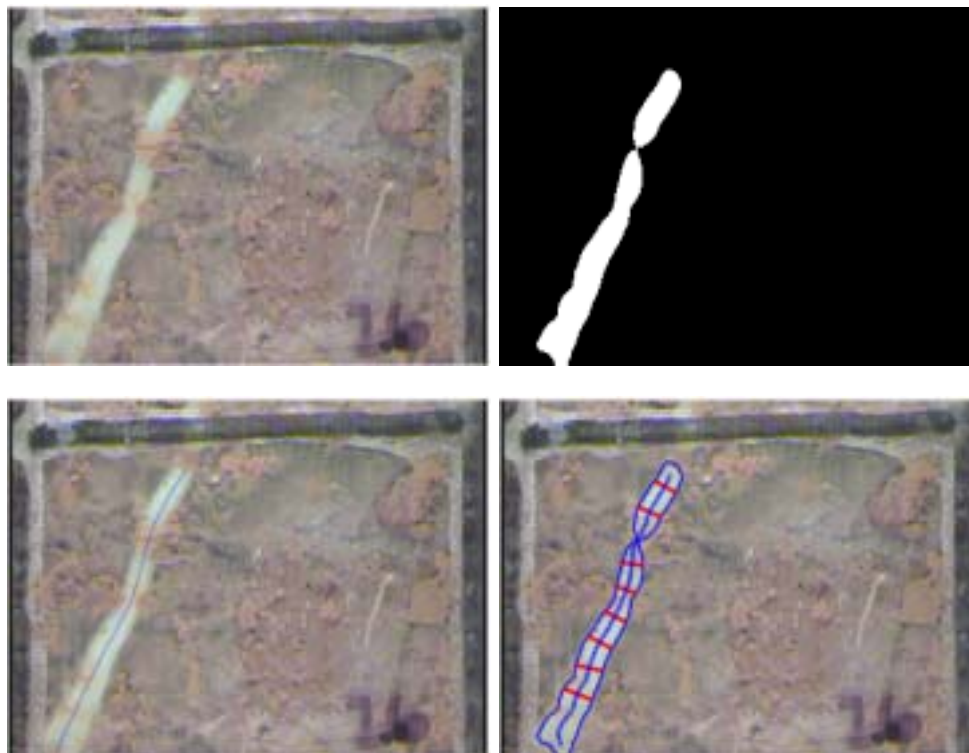


Figure 4.1: The results of applying our approach to 12 sample images. First row: Input Image and Extracted root; Second row: Hand-labeled medial axis and measured root. (cont.)

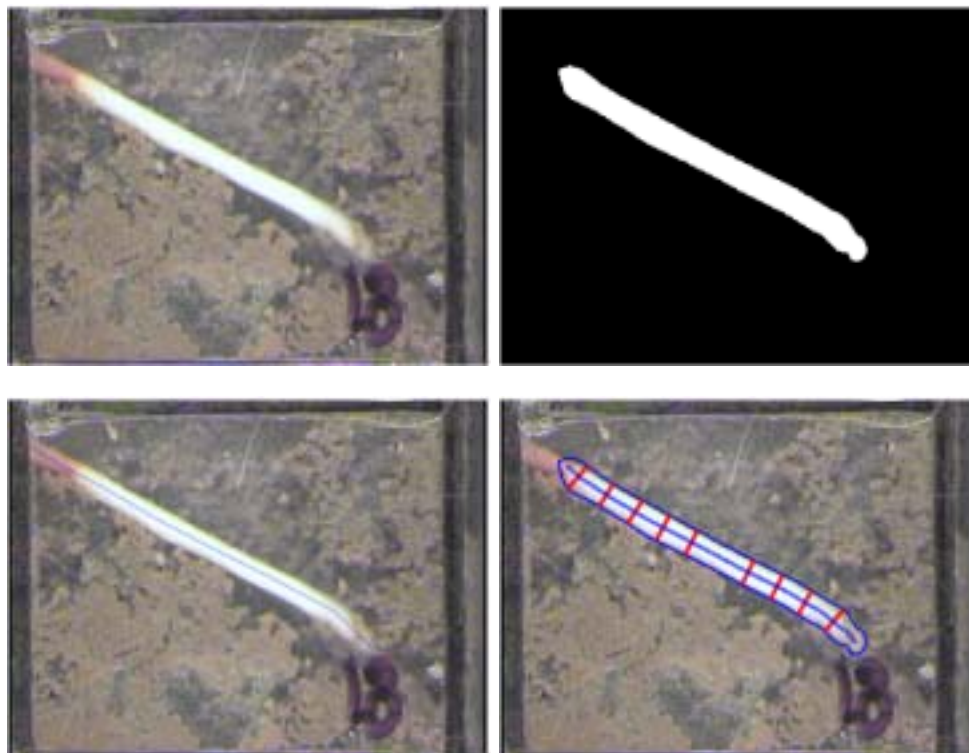


Figure 4.1: The results of applying our approach to 12 sample images. First row: Input Image and Extracted root; Second row: Hand-labeled medial axis and measured root. (cont.)

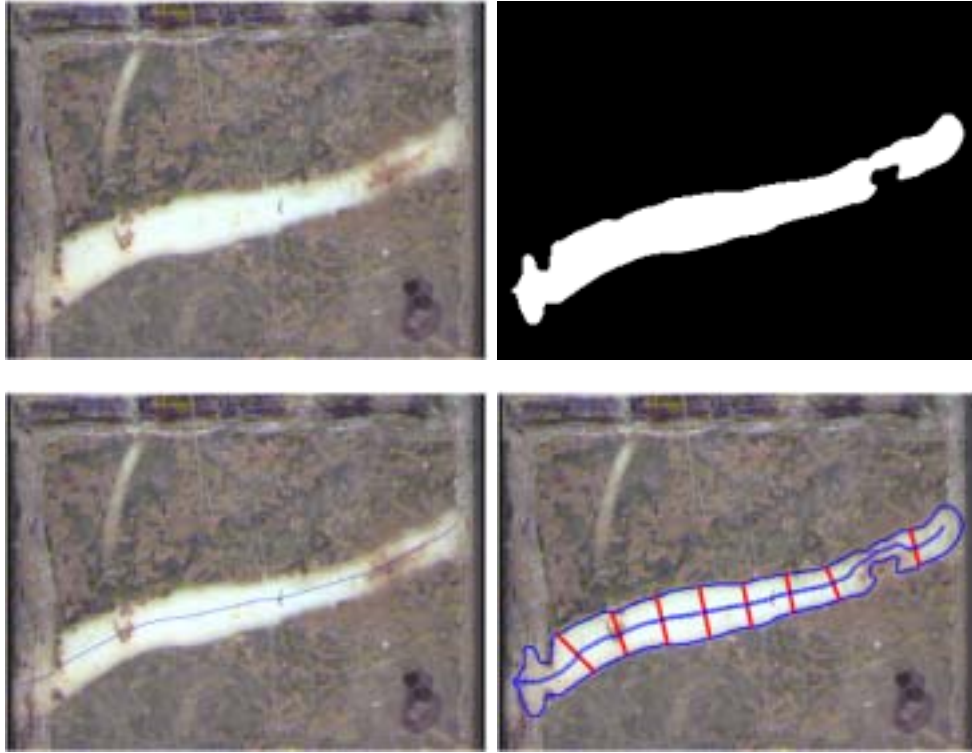


Figure 4.1: The results of applying our approach to 12 sample images. First row: Input Image and Extracted root; Second row: Hand-labeled medial axis and measured root. (cont.)

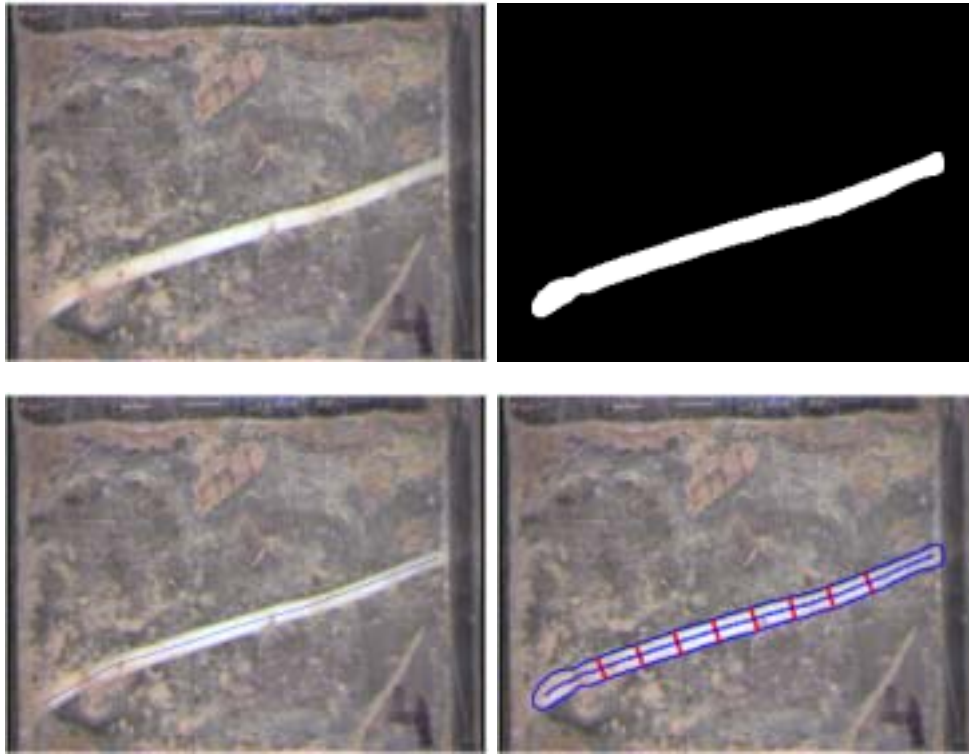


Figure 4.1: The results of applying our approach to 12 sample images. First row: Input Image and Extracted root; Second row: Hand-labeled medial axis and measured root. (cont.)

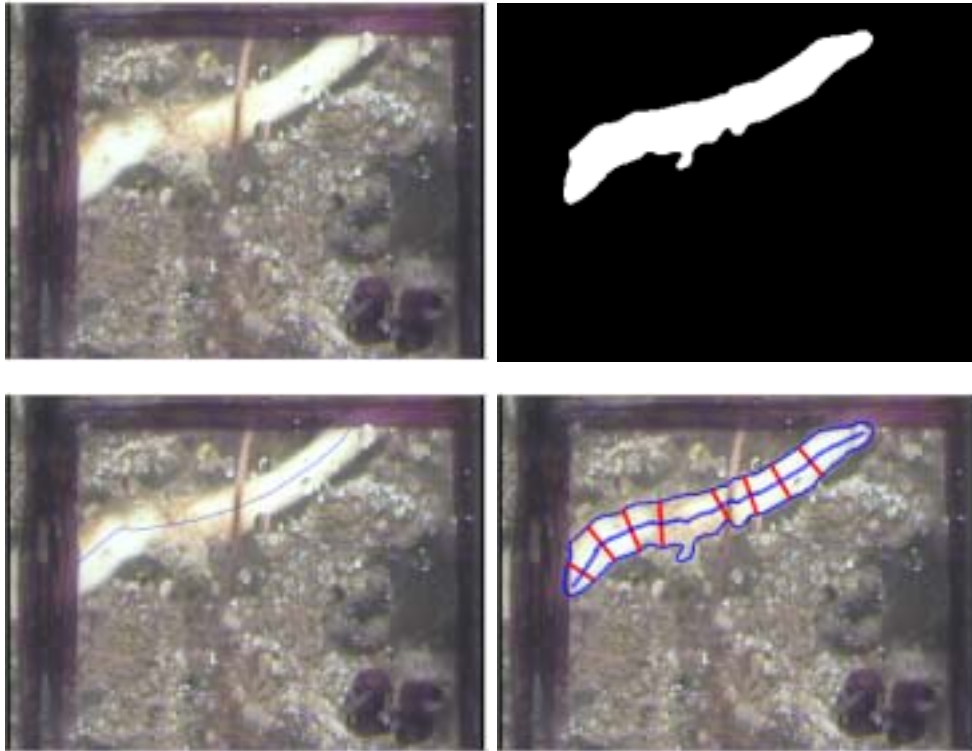


Figure 4.1: The results of applying our approach to 12 sample images. First row: Input Image and Extracted root; Second row: Hand-labeled medial axis and measured root. (cont.)

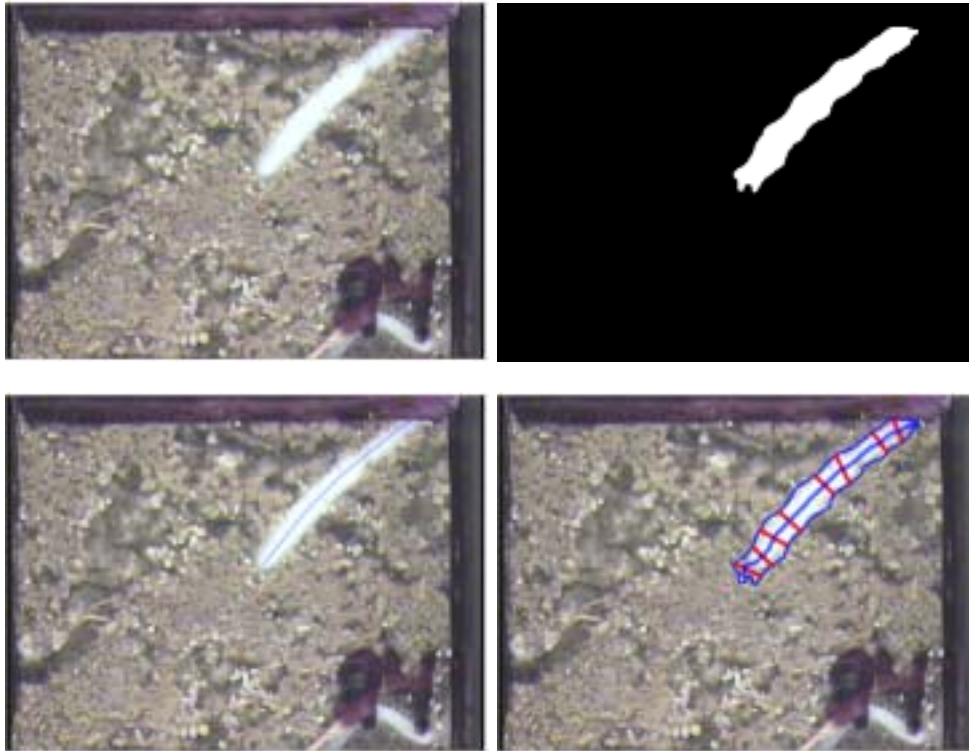


Figure 4.1: The results of applying our approach to 12 sample images. First row: Input Image and Extracted root; Second row: Hand-labeled medial axis and measured root. (cont.)

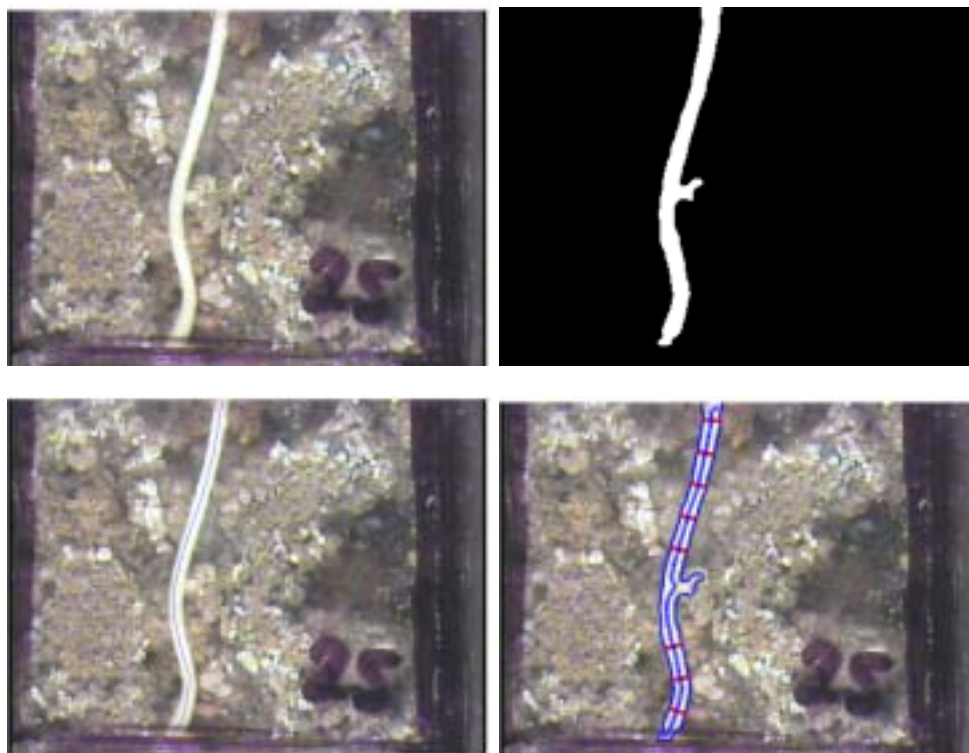


Figure 4.1: The results of applying our approach to 12 sample images. First row: Input Image and Extracted root; Second row: Hand-labeled medial axis and measured root. (cont.)

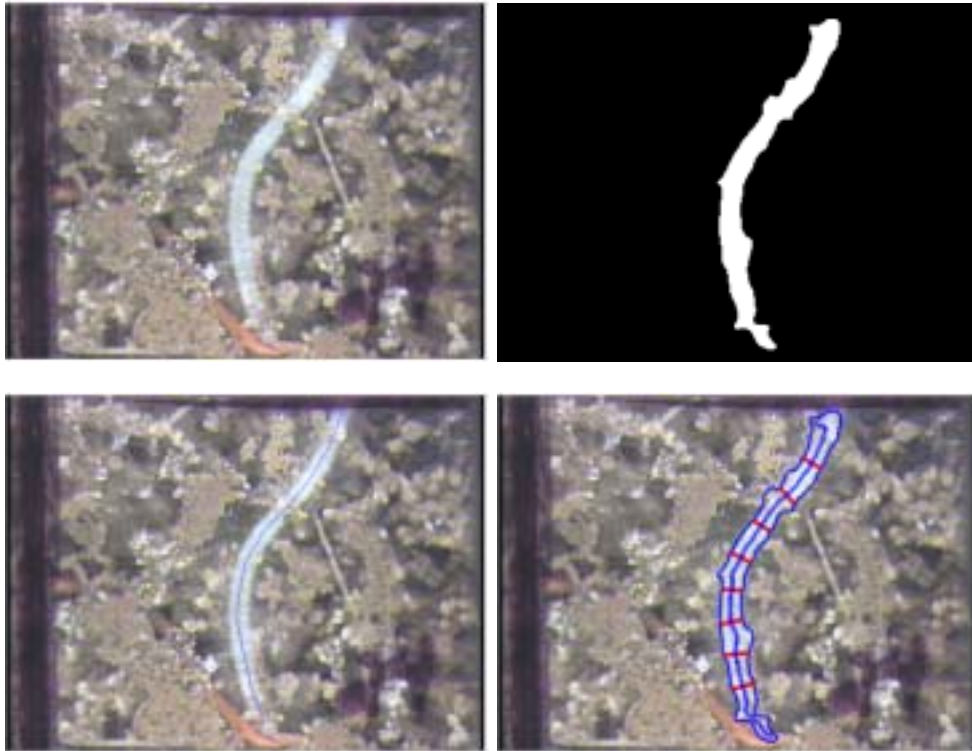


Figure 4.1: The results of applying our approach to 12 sample images. First row: Input Image and Extracted root; Second row: Hand-labeled medial axis and measured root. (cont.)

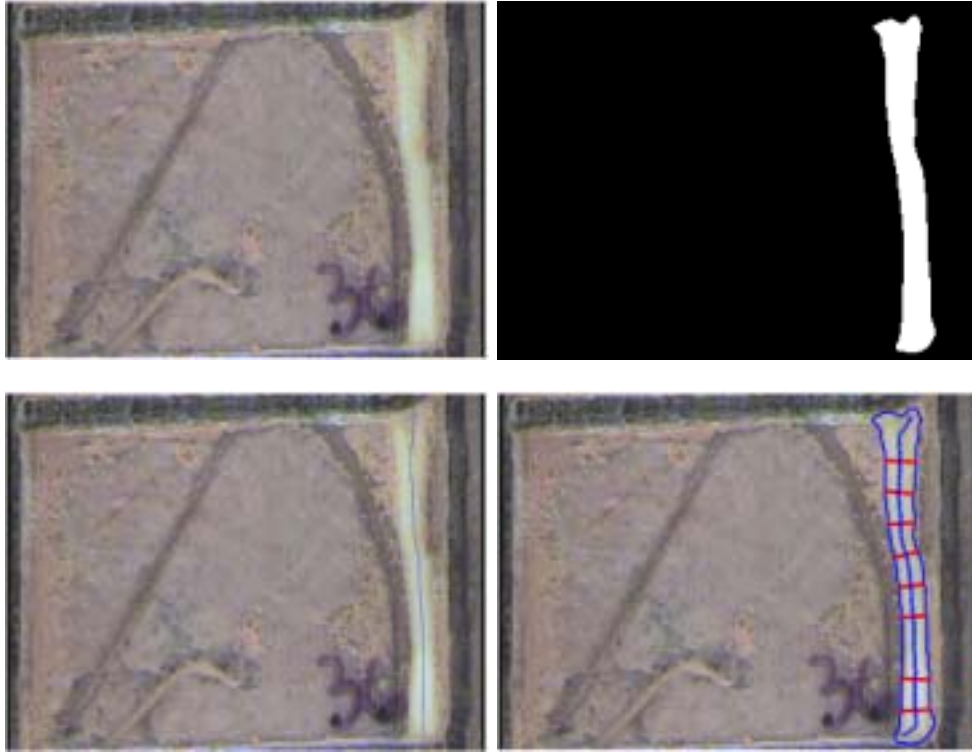


Figure 4.1: The results of applying our approach to 12 sample images. First row: Input Image and Extracted root; Second row: Hand-labeled medial axis and measured root. (cont.)

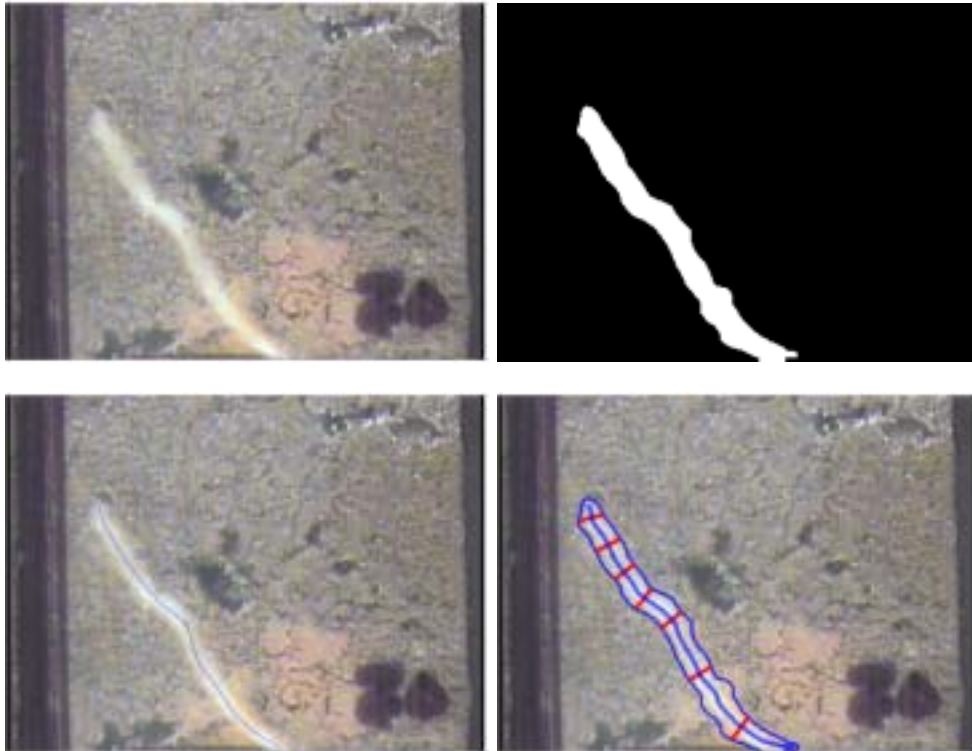


Figure 4.1: The results of applying our approach to 12 sample images. First row: Input Image and Extracted root; Second row: Hand-labeled medial axis and measured root. (cont.)

histogram based approach, Otsu's method just considers the overall gray level statistics of the image and does not involve the spatial relationship of the pixels, it works well only if the histogram of the MFR image exhibits a good bimodal distribution. Unlike Otsu's method, the local entropy thresholding method measures the two-dimensional grayscale distribution and considers the relationship of grayscale statistics of the neighboring pixels. So when the MFR image has some complicated relationship or overlap between foreground and background, the local entropy thresholding method yields a better result than Otsu's method. A comparison between Otsu's method and local entropy thresholding method is shown in [Figure 4.2](#).

The Freeman formula and Pythagorean theorem are also widely used length estimators in root measurement. Here, we compare their performance with Kimura's method. Twenty roots are selected from our database and measured by the three methods. We evaluated their accuracy by comparing the deviation of the calculated length to the hand-measured reference length ([Figure 4.3](#)). The deviation equation is:

$$\text{Measurement Deviation} = \frac{\text{Calculated Length} - \text{Reference Length}}{\text{Reference Length}} \times 100\% \quad (4.1)$$

The results are shown in [Table 4.1](#). Compared with Freeman formula, Kimura's method significantly minimizes the effect of root orientation and size on measurement accuracy. The average measurement bias reduces from 7.99% to 4.56%. Also as shown in [Figure 4.4](#), a highly significant correlation ($r^2 = 0.9286$) is obtained between Kimura's method measured root length and the manually measured reference length, while the correlation between Freeman's equation and the manually measurement of length is only 0.893. In [Figure Table 4.1](#), we also observe an interesting phenomenon that the performance of the Pythagorean theorem is better than the performance of Kimura's method. The reason is that most roots we chose to use for this test contain a single line medial axis, for which the Pythagorean theorem is more accurate. When applied to measuring root with multi-line

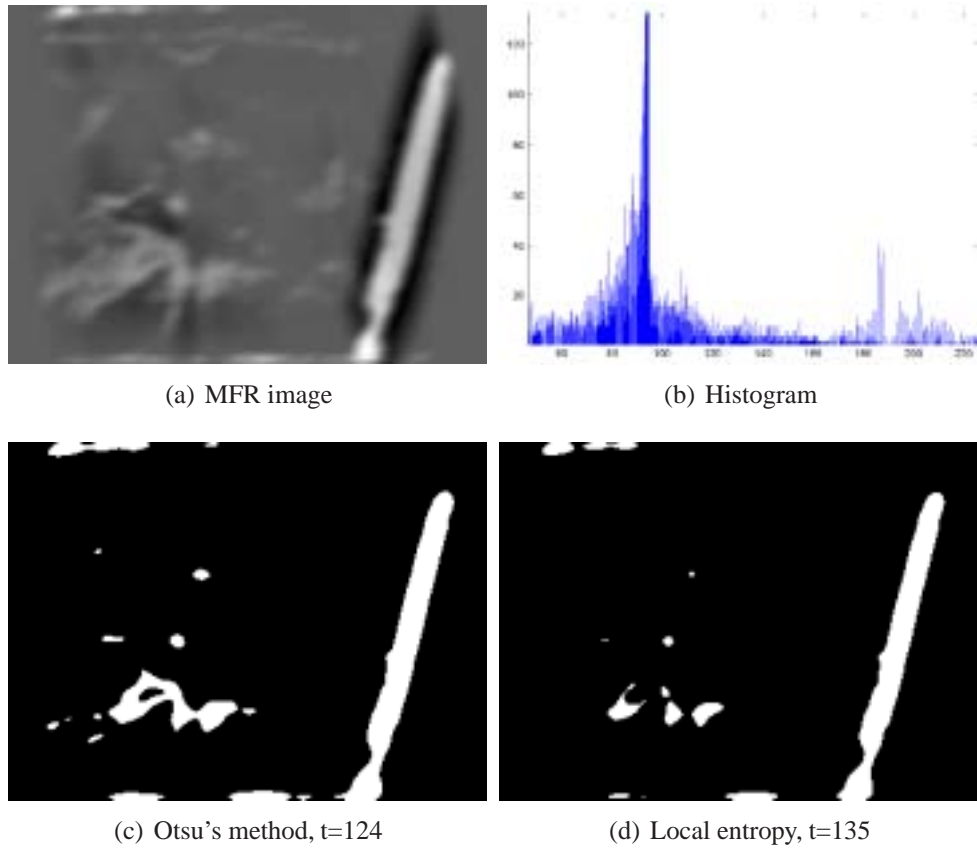


Figure 4.2: In this MFR image, the histogram exhibits a bimodal distribution, so both of the two methods work well.

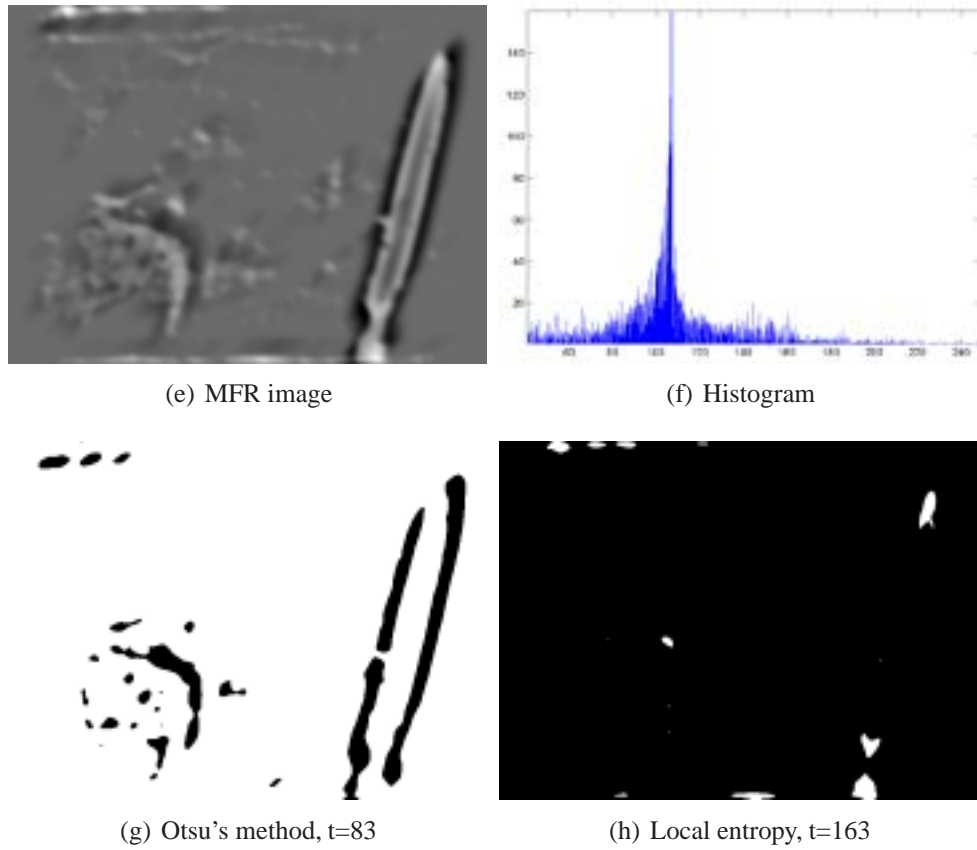


Figure 4.2: In this MFR image, the histogram exhibits unimodal distribution. Otsu's method fails while the LET method works well. (cont.)

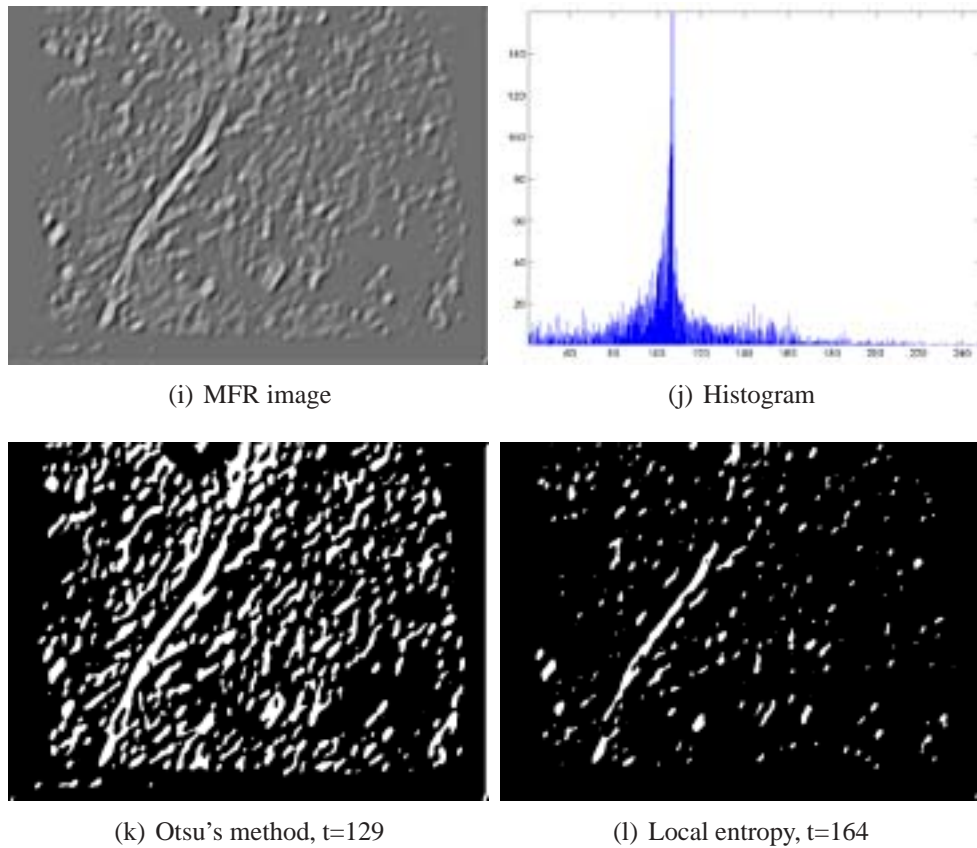


Figure 4.2: In this MFR image, the histogram exhibits a complicated relationship between foreground and background. The output of Otsu's method has severe shape distortion, while the LET method gives a better result. (cont.)

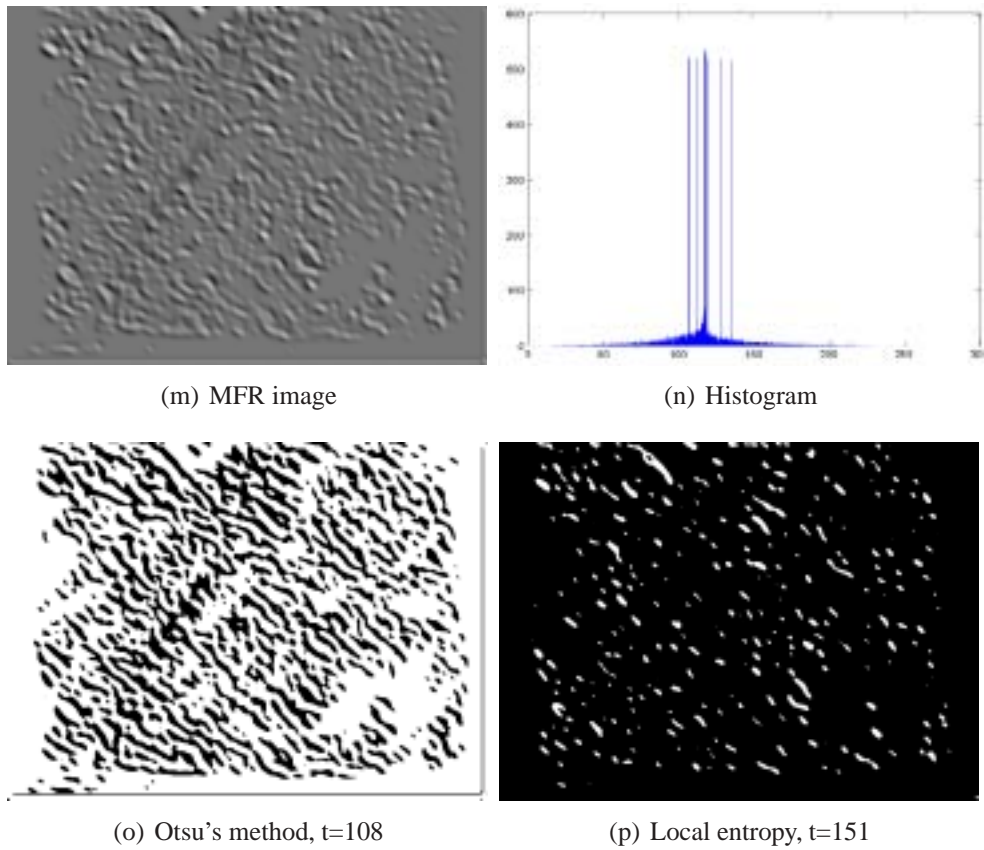


Figure 4.2: In this MFR image, the histogram exhibits a complicated relationship between foreground and background. The Otsu's method fails while the LET method works well. (cont.)

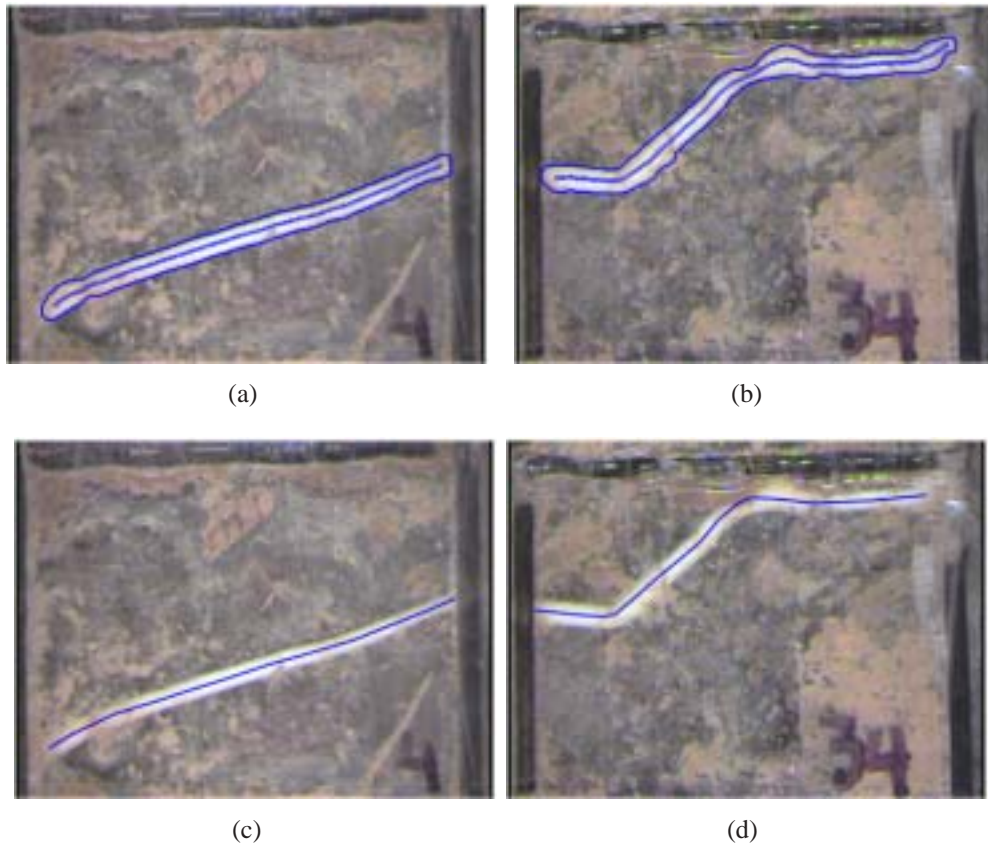


Figure 4.3: Sample Roots used for the experiment. First row: The medial axis used for root length measurement; Second row: The hand-labeled ground truth used for reference length.

medial axis as shown in Figure 4.3(b), its accuracy will substantially decrease. For the measurement of Figure 4.3(b), the measurement deviation of the Pythagorean theorem is 3.68%, while that of our method is only 1.11%.

Measurement Deviation (%)	Max	Min	Avg
Freeman Formula	17.99	0.296	7.99
Pythagorean theorem	11.63	0.283	4.22
Kimura's Method	14.43	0.075	4.56

Table 4.1: Comparison among these three methods.

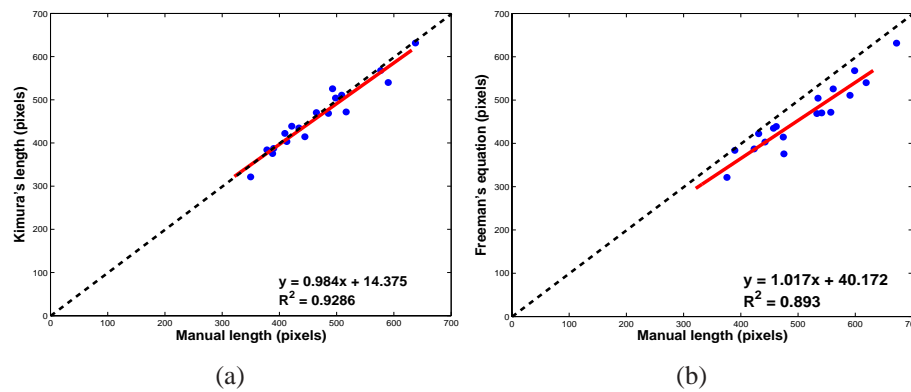
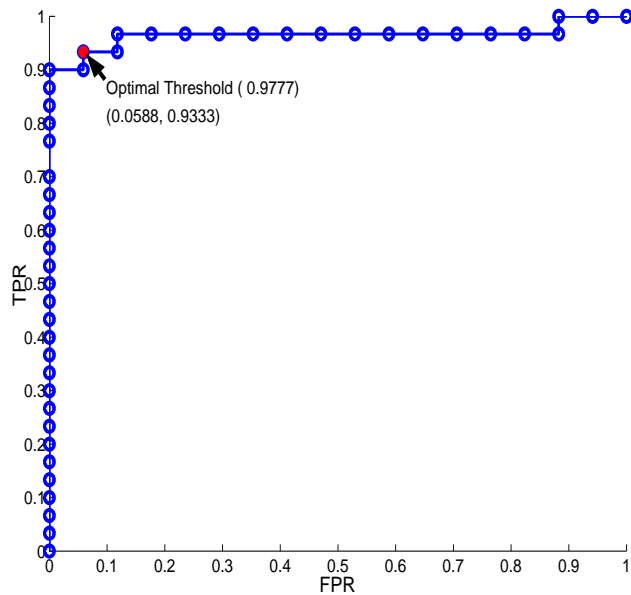


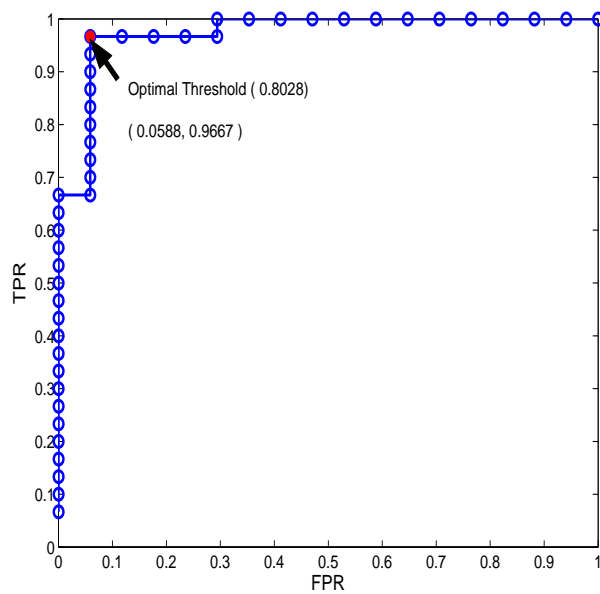
Figure 4.4: (a) Relationship between root length determined by Kimura's method and manual measurement; (b) Relationship between root length determined by Freeman formula and manual measurement.

In chapter 3, we presented five methods to discriminate roots and construct ROC curves to estimate the optimal threshold value for each method. In our experiment, there is total of 47 objects detected in the 45 minirhizotron images; 30 of them are root. So, the number of root in the images is 30, the number of no-root objects in the images is 17. The experiment results are shown in Figure 4.5 and Table 4.2.

The ROC curve also can be used to judge the discrimination ability of each method. As summarized in [26], the larger the area beneath an ROC curve, the more accurate the method. Meanwhile, the closer the optimal threshold point to the point (0,1), the more accurate the method. After carefully comparing the ROC curves, we conclude that the

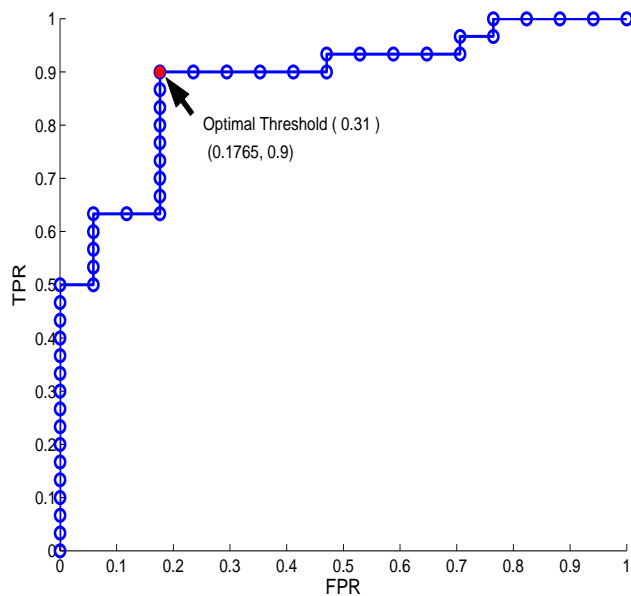


(a) The eccentricity method

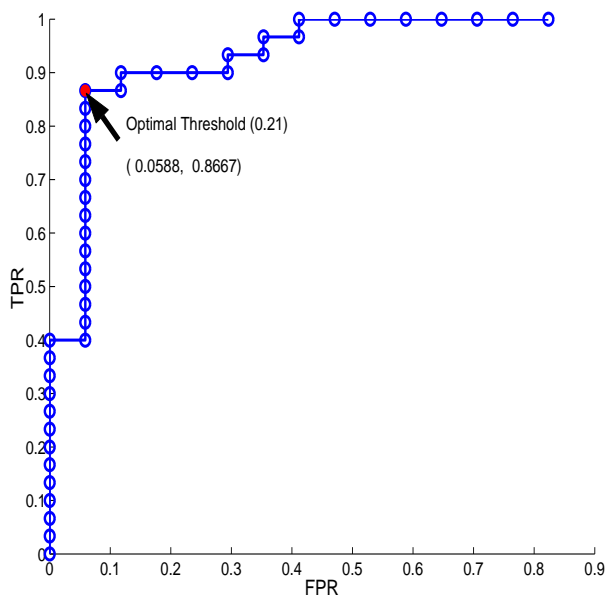


(b) The approximate line symmetry method

Figure 4.5: The ROC curve and the estimated optimal thresholding value of each method.

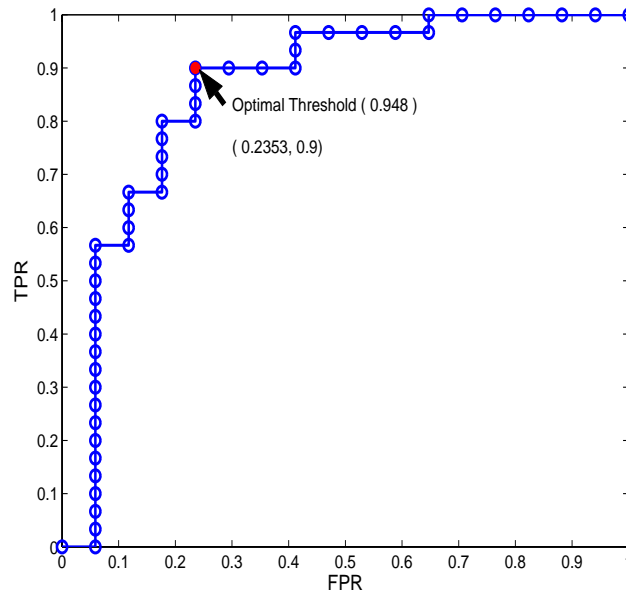


(c) The boundary parallelism method



(d) The histogram distribution method

Figure 4.5: The ROC curve and the estimated optimal thresholding value of each method. (cont.)



(e) The edge detection method

Figure 4.5: The ROC curve and the estimated optimal thresholding value of each method. (cont.)

Method	TPR	FPR
Eccentricity	0.933	0.059
Approximate Line Symmetry	0.967	0.059
Parallel Boundary	0.9	0.176
Histogram Distribution	0.867	0.059
Edge Detection	0.9	0.235

Table 4.2: TPR and FPR of the five methods at the optimal thresholding point.

approximate line symmetry method performs better than other four methods, based on the observation that the ROC curve of the approximate line symmetry method covers the largest area (Figure 4.6) and the distance from its optimal threshold point to the point (0,1) is the shortest (Table 4.3).

As mentioned earlier, a limitation of our approach is that it is restricted to no more than one root per image. We experimented with a simple technique to handle up to two roots per image. In each thresholded binary image, we chose the two largest components as the root candidate in the root selecting step, and then ran our root discriminating algorithm. The

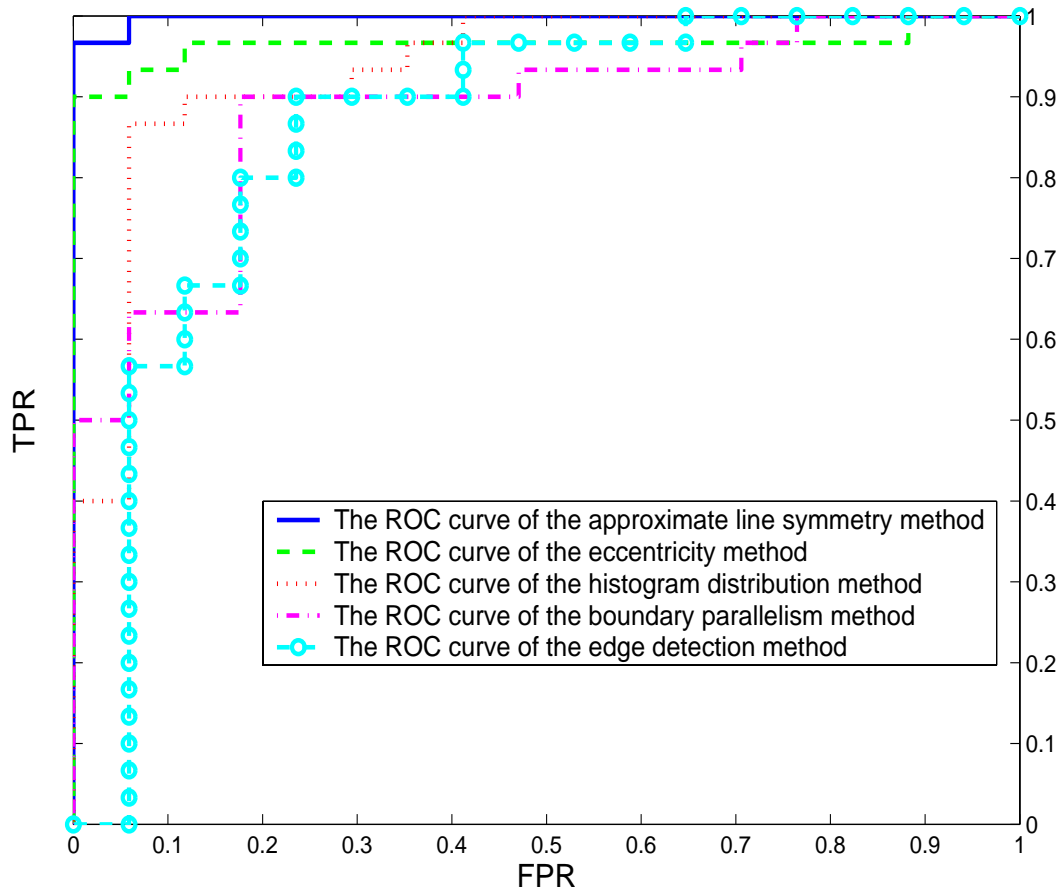


Figure 4.6: ROC curves of the five methods

Method	Dist to point(0,1)
Eccentricity	0.0889
Approximate Line Symmetry	0.0676
Parallel Boundary	0.2028
Histogram Distribution	0.1457
Edge Detection	0.2557

Table 4.3: The distances between the optimal threshold point of the five methods to the ideal point (0,1).

experimental results show that this method works well on some of the root images, but the false positive rate is substantially increased to 14% (more bright background objects are misclassified in the no-root images). Some examples are shown in [Figure 4.7](#)

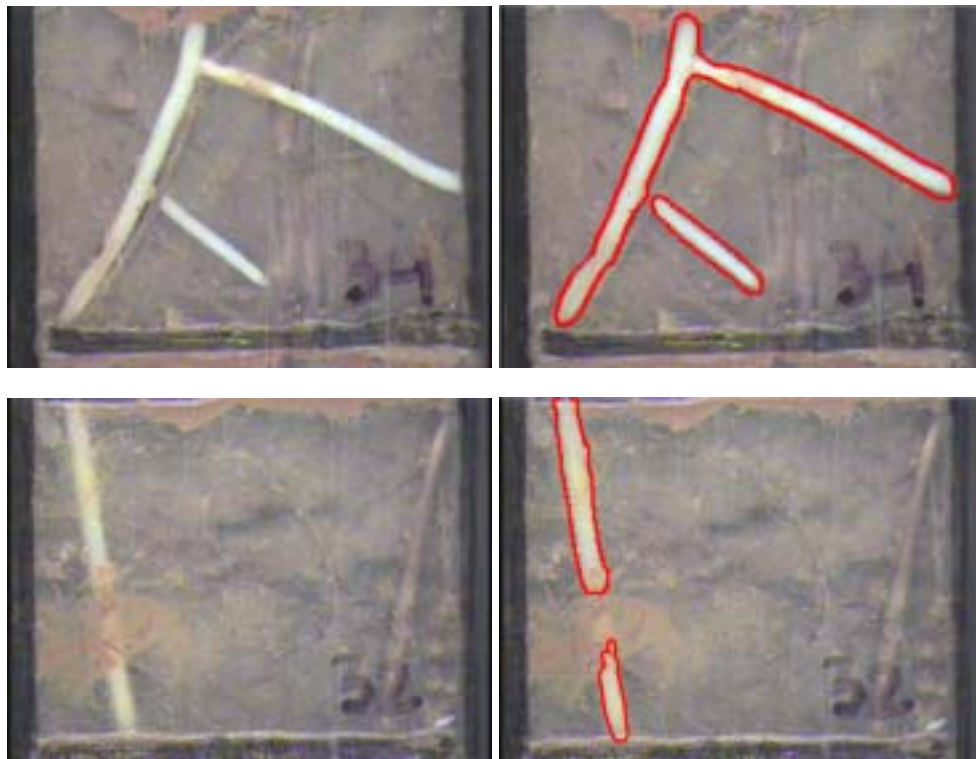


Figure 4.7: Examples of multiple roots detection.

Chapter 5

Conclusion

Automatic analysis of minirhizotron root images is very important for studying roots. In this thesis we describe a new approach to automatically detect and measure roots in minirhizotron images. The approach includes five advantages: (1) It works on multiple root types in a variety of soil types, (2) It uses a robust thresholding method for root extraction, (3) It lessens the shape distortion using individual matched filters outputs for thresholding, (4) It robustly detects the medial axis using Dijkstra's algorithm, and it provides accurate methods for root/no-root discrimination. We tested our methods on a set of 45 minirhizotron images containing different sizes of roots as well as those containing no root or dead roots. Our overall correct detection rate is 96.7% and the false positive rate is 0.06%. Our root length estimator can measure root length within 4.56% error.

This research is far from complete at this time. There are many avenues available for future work. The major limitation of this approach is the burdensome computation of matched filtering. On a Windows XP, Pentium 4, CPU 2.8 GHz, using MATLAB version 6.5.1, the presented approach requires 42 minutes to process a 640×480 pixel images. Because Matlab language proceeds loops very slowly, implementing our approach in C language should substantially decrease the computation time. Another method that may help to solve this problem is multiple subsampling. One could repeatedly reduce the image

size by subsampling and convolving with a set of smaller sized match filter for local contrast enhancement. This will be another opportunity for future work.

In our research, we explore five methods to discriminate roots against bright extraneous objects. Among these methods, the approximate line symmetry method performs the best. However, the other four methods also have their own advantages. Properly combining them would improve the accuracy of root discrimination. Also, our present approach is constrained to detect one root per image, while lots of minirhizotron images contain multiple roots. Therefore, one important avenue of future research would be to seek an optimal combination of these techniques and to extend the approach to handle multiple roots per image.

Bibliography

- [1] O. Andren, H. Elmquist, and A. Hansson, Recording, processing and analysis of grass root images from a rhizotron. *Plant and Soil*, vol. 185, no. 2, pp. 259–264, 1996.
- [2] T. Chanwimaluang and G. Fan, An efficient blood vessel detection algorithm for retinal images using local entropy thresholding. In *Proceeding of the IEEE International Symposium on Circuits and Systems*, vol. 5, pp. 21–24, 2003.
- [3] S. Chaudhuri, S. Chatterjee, N. Katz, M. Nelson, and M. Goldbaum, Detection of blood vessels in retinal images using two-dimensional matched filters. *IEEE Transactions on Medical Imaging*, vol. 8, no. 3, pp. 263–269, 1989.
- [4] W. Cheng, D. Colemanand, and J. Box, Measuring root turnover using the minirhizotron technique. *Agriculture, Ecosystems and Environment*, vol. 34, pp. 261–267, 1991.
- [5] T. Cormen, C. Leiserson, R. Rivest, and C. Stein, Introduction to Algorithms 2nd Edition. McGraw–Hill, 2001.
- [6] L. Dorst and A. Smeulders, Length estimators for digitized contours. *Computer Vision, Graphics, and Image Processing*, vol. 40, pp. 311–333, 1987.
- [7] R. Dowdy, A. Smucker, M. Dolan, and J. Ferguson, Automated image analyses for separating plant roots from soil debris elutriated from soil cores. *Plant and Soil*, vol. 200, no. 1, pp. 91–94, 1998.
- [8] B. Eghball, J. Settimi, J. Maranville, and A. Parkhurst, Fractal analysis for morphological description of corn roots under nitrogen stress. *Agronomy Journal*, vol. 85, no. 2, pp. 287–289, 1993.
- [9] G. Erz and S. Posch, A region based seed detection for root detection in minirhizotron images. http://users.informatik.uni-halle.de/~erz/erz_posch_seeddetection.pdf
- [10] H. Freeman, Boundary encoding and processing. Picture processing and psychopictorics, pp. 241–266, Academic Press, 1970.
- [11] C. Glasbey and G. Horgan, Image Analysis for the biological sciences, Wiley–Sons, 1995.

- [12] R. Gonzalez and R. Woods, *Digital Image Processing*, 2nd Edition, Prentice–Hall, 2002.
- [13] R. Hendrick and K. Pregitzer, Patterns of fine root mortality in two sugar maple forests. *Nature*, vol. 361, pp. 59–61, 1993.
- [14] R. Hendrick and K. Pregitzer, Applications of minirhizotrons to understand root function in forests and other natural ecosystems. *Plant and Soil*, vol. 185, no.2, pp. 293–304, 1996.
- [15] A. Hoover, V. Kouznetsova, and M. Goldbaum, Locating blood vessels in retinal images by piecewise threshold probing of a matched filter response. *IEEE Transactions on Medical Imaging*, vol. 19, no. 3, pp. 203–210, 2000.
- [16] K. Kimura, S. Kikuchi, and S. Yamasaki, Accurate root length measurement by image analysis. *Plant and Soil*, vol. 216, no. 1, pp. 117–127, 1999.
- [17] Z. Kulpa, Area and perimeter measurement of blobs in discrete binary pictures. *Computer Vision, Graphics, and Image Processing*, vol. 6, pp. 434–454, 1977.
- [18] R. Lebowitz, Digital image analysis measurement of root length and diameter. *Environmental and Experimental Botany*, vol. 28, pp. 267–273, 1988.
- [19] A. Mackay and S. Barber, Effect of nitrogen on root growth of two corn genotypes in the field. *Agronomy Journal*, vol. 78, no. 4, pp. 699–703, 1986.
- [20] S. Murphy and A. Smucker, Evaluation of video image analysis and line-intercept methods for measuring root systems of alfalfa and ryegrass. *Agronomy Journal*, vol. 87, no. 5, pp. 865–868, 1995.
- [21] A. Nater, D. Nater, and M. Baker, Application of artificial neural system algorithms to image analysis of roots in soil. I. Initial results. *Geoderma*, vol. 53, no. 3, pp. 237–253, 1992.
- [22] N. Otsu, A threshold selection method from gray level histograms. *IEEE Transactions on Systems, Man, and Cybernetics*, vol. 9, no. 1, pp. 62–66, 1979.
- [23] R. Pajak, Use of two-dimensional matched filters for estimating a length of blood vessels newly created in angiogenesis process. *Opto-Electronics Review*, vol. 11, no. 3, pp. 237–241, 2003.
- [24] N. Pal and S. Pal, Entropic thresholding. *Signal processing*, vol. 16, pp. 97–108, 1989.
- [25] G. Patena and K. Ingram, Digital acquisition and measurement of peanut root minirhizotron images. *Agronomy Journal*, vol. 92, no. 3, pp. 541–544, 2000.
- [26] J. Swets, Measuring the accuracy of diagnostic systems. *Science*, vol. 240, pp. 1285–1293, 1988.
- [27] J. Thomas and T. Cover, *Elements of Information Theory*, Wiley–Sons 1991.

- [28] T. Vamerali, A. Ganis, S. Bona, and G. Mosca, An approach to minirhizotron root image analysis. *Plant and Soil*, vol. 217, no. 1, pp. 183–193, 1999.
- [29] T. Vamerali, M. Guarise, A. Ganis, S. Bona, and G. Mosca, Analysis of root images from auger sampling with a fast procedure: a case of application to sugar beet. *Plant and Soil*, vol. 255, no. 1, pp. 387–397, 2003.
- [30] D. Upchurch and J. Ritchie, Root observations using a video recording system in mini-rhizotrons. *Agronomy Journal*, vol. 75, no. 6, pp. 1009–1015, 1983.